Supramolecular Self-Assembled Multi-Electron-Acceptor Organic Molecule as High-Performance Cathode Material for Li-Ion Batteries

Meng-Siou Wu, Teng-Hao Chen, Hailong Lyu, Te-Wei Huang, Sheng Dai, Xiao-Guang Sun, Alexander S. Ivanov, Jui-Chin Lee, Ilja Popovs, and Watchareeya Kaveevivitchai**

M.-S. Wu, Prof. Dr. W. Kaveevivitchai
Department of Chemical Engineering
Hierarchical Green-Energy Materials (Hi-GEM) Research Center
National Cheng Kung University
Tainan City 70101, Taiwan
Email: wkaveechai@mail.ncku.edu.tw

Prof. Dr. Teng-Hao Chen
School of Pharmacy
National Cheng Kung University
Tainan City 70101, Taiwan

Dr. H. Lyu, Prof. Dr. S. Dai, Dr. X.-G. Sun, Dr. A. S. Ivanov, Dr. I. Popovs
Chemical Sciences Division
Oak Ridge National Laboratory
Oak Ridge, P.O. Box 2008, TN 37831, USA
E-mail: popovsi@ornl.gov

Te-Wei Huang
Department of Chemistry
Tamkang University
New Taipei City 25137, Taiwan

Jui-Chin Lee
Instrument Center
National Cheng Kung University
Tainan City 70101, Taiwan

Keywords: organic cathode materials, supramolecular assemblies, Li-ion batteries

Abstract: Organic electrode materials possess many advantages such as low toxicity, sustainability, and chemical/structural tunability toward high energy density. However, to compete with inorganic-based compounds, crucial aspects such as redox potential, capacity, cycling stability, and electronic conductivity need to be improved. Herein, we report a comprehensive strategy on the molecular design of small organic electron-acceptor-molecule — hexaazatrianthranylene (HATA) embedded quinone (HATAQ). By introducing conjugated

quinone moieties into the electron-deficient hexaazatriphenylene-derivative core, HATAQ with highly extended π-conjugation can yield extra-high capacity for lithium storage, delivering a capacity of 426 mAh g^{-1} at 200 mA g^{-1} (0.4C). At an extremely high rate of 10 A g^{-1} (19C), a reversible capacity of 209 mAh g^{-1} corresponding to nearly 85% retention is obtained after 1000 cycles. A unique network of unconventional lock-and-key hydrogen bonds in the solid state facilitates favorable supramolecular 2D layered arrangement, enhancing cycling stability. To the best of our knowledge, the capacity and rate capability of HATAQ are found to be the best ever reported for organic small-molecule-based cathodes. These results together with density functional theory (DFT) studies provide proof-of-concept that our design strategy is promising for the development of organic electrodes with exceptionally high energy density, rate capability, and cycling stability.

1. Introduction

An ever-increasing demand for grid energy storage due to the advent of intermittently available renewable energy sources and the global desire to avoid the most destructive consequences of the climate change led to an exponential growth of research into alternative and sustainable battery technologies.[1–4] While transition-metal-based inorganic compounds have been primarily used as cathodes, especially in Li-ion batteries (LIBs), the pace of the development of organic electrode materials continues to accelerate.[2] Organic compounds are considered to be more environment-friendly compared to their inorganic counterparts. They are also composed of light and naturally abundant elements (C, H, N, O, and S) eliminating the need for expensive and toxic metals, and can be prepared directly from renewable resources or synthesized from readily available small molecules. As a result, organic electrode materials could reduce the energy consumption and CO_2 release during mass production, unlike materials

containing transition metals which come from exhaustible mineral resources and require intensive mining, processing, and disposal.

Small-molecule organic compounds can be rationally designed and synthesized with high precision to contain well-defined redox-active functional groups. Due to this unparalleled chemical and structural tunability, a large number of redox active sites can be incorporated in a single molecule, potentially leading to high practical capacity.[5] The redox potential of organic electrode materials can be fine-tuned at the molecular level by introducing electron-withdrawing or electron-donating functional groups into the conjugated structure in order to increase or decrease the potential, respectively. Therefore, organic compounds can be engineered to act as either cathode or anode materials, depending on the desired application.[6] Furthermore, the majority of organic compounds are able to offer fast reaction kinetics as well as facile processing due to relatively flexible structures compared to the inorganic counterparts.

So far, a number of diverse structural motifs have been investigated as organic cathode materials in rechargeable LIBs, namely, conjugated polycarbonyl compounds,[7–11] conducting polymers,[12] persistent radical derivatives,[13–15] organosulfur derivatives,[16–19] and redox-active heterocycles,[20–22] which have particularly shown great promise. However, in most organic electrodes, issues associated with low electronic conductivity and material dissolution in typical organic solvents, used in electrolytes alongside lithium salt, generally result in poor cycling performance, rapid capacity fading as well as low Coulombic efficiency.[23]

Several strategies have been devised to address the dissolution problem of small molecule-based materials, such as anchoring electroactive species onto polymeric[24] or other conductive materials (i.e., carbon nanotubes) via polymerization or post-synthetic functionalization.[25] Salting is another strategy that has been utilized for this purpose.[26] Additional strategies such as increasing the size of aromatic systems has

been attempted to both decrease the solubility of the material via enhanced π-π stacking as well as to improve electronic conductivity.[27] Oftentimes, however, these strategies result in an increase in the molecular weight of the electroactive materials leading to low energy density, due to an increase in the unit weight per electron uptake. Additionally, this leads to creating densely packed crystalline solids with poor lithium transport. Therefore, novel structural design strategies toward the development of small molecule-based organic electrode materials capable of providing high energy density, high rate capability, and outstanding stability are needed.

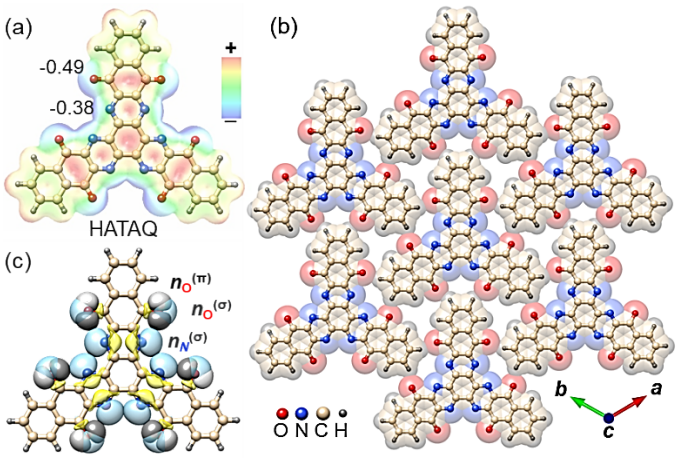

Figure 1. (a) Chemical structure of HATAQ with plotted electrostatic potential map (0.005 e/a_0^3 isovalue) and charges on O and N atoms obtained from natural population analysis. (b) Single-crystal structure of the 2D layer of HATAQ molecules stitched together by lock-key C—H···O bonds. Solvent molecules and adjacent HATAQ layers along the *c*-direction are not shown for clarity. (c) s-type, $n^{(\sigma)}$, and p-type, $n^{(\pi)}$, lone pairs of HATAQ revealed by natural bond orbital analysis.

Inspired by the recent progress on multi-electron-acceptor small-molecule triquinoxalinylene (3Q),[28] also known as 5,6,11,12,17,18-hexaazatrinaphthyl-ene (HAT),[29] with multiple electroactive pyrazine units capable of high-capacity lithium storage, we envisioned that a holistic 3-prong (supra)molecular design strategy could be effective in increasing the number of functional groups and facilitating favorable solid state organization that enhances electrode cycling stability and performance. As a

starting point, we used hexaazatrianthranylene (HATA) moiety (SI, **Scheme S2**) as an electron-deficient core structure, mainly due to its highly reversible electrochemical behavior and π-extended structure containing heteroatoms with lone pair electrons, which is believed to allow more efficient electron transfer processes, thus promoting conductivity.[30] Various carbonyl-containing structures due to their electron-withdrawing properties have been shown to enable the tailoring of materials with high redox potential, which is one of the important criteria in the design of high-performance cathodes. Therefore, we considered that by introducing a conjugated quinone moiety into the structure of HATA to yield HATAQ (shown in **Figure 1a**), the electrochemical reduction potential of HATAQ could be increased in combination with the electron withdrawing nature of the HATA azacycle.[31] This, as a consequence, results in better orbital overlap and additional coordination sites for lithium ions upon reduction.

Herein we report a design strategy and comprehensive study on the performance of the new addition to the family of high-performance small-molecule organic cathode materials—HATAQ. This peculiar material is found to behave excellently as cathode in rechargeable organic batteries with more extended π-conjugation and larger number of redox active sites, facilitating charge transport and yielding extra-high capacity for lithium storage. Additionally, rigid, relatively flat and trigonal geometry decorated with strong hydrogen-acceptor oxygen atoms present in HATAQ structure, together with the polarized C—H bonds leads to multiple unconventional C—H···O interactions, thus stabilizing the supramolecular superstructure in the solid state (**Figure 1b**). Several experimental characterization techniques in combination with density functional theory (DFT) studies shed light on the mechanism of HATAQ redox behavior during lithiation process, confirming the highly reversible nature of multi-electron reaction.

2. Results and Discussion

2.1. Molecular Design of HATAQ

Based on our retrosynthetic analysis, we have devised a straightforward synthesis scheme to obtain the desired HATAQ heterocycle, starting from cheap and readily available starting materials (SI, **Scheme S2**). Triple condensation between cyclohexane hexaketone and 2,3-diamino-1,4-naphthaquinone in acetic acid at 60 °C for 12 h afforded the desired compound in excellent yield. The ease of synthesis was exemplified by scaling up the reaction to produce more than 50 g of HATAQ material in a single reaction. The as-synthesized HATAQ contained some residual water as indicated by thermogravimetric analysis (TGA) of the sample after vacuum drying at room temperature (**Figure S3**). In order to obtain the solvent-free material, it had to be heated at 120 °C for 24 h under high vacuum. Chemical composition of the HATAQ was confirmed using a variety of spectroscopic methods (see SI for details).

To gain insight into the redox properties of the synthesized compound, we performed quantum chemical calculations using density functional theory (DFT). As expected, the presence of additional electron-withdrawing carbonyl groups in the HATAQ structure substantially lowered the energy level (-3.92 eV) of the lowest unoccupied molecular orbital (LUMO) as compared to the LUMO of 3Q (-2.97 eV) [28] calculated at the same level of theory. This indicates that HATAQ should possess superior electron affinity and thus higher reduction potential. In addition, the HOMO-LUMO energy gap, E_g, was calculated to be 3.74 eV (**Figure S15**), which is on par with E_g (3.66 eV) for 3Q molecule, [28] suggesting sufficient intrinsic electronic conductivity of HATAQ. Furthermore, the electrostatic potential map of the HATAQ molecule in **Figure 1a** clearly shows the highly electronegative regions formed by the carbonyl oxygen and imine nitrogen groups constituting the ideal chelating sites suitable for lithium binding and storage. Lone pair natural bond orbitals (NBO) on the corresponding oxygen and nitrogen donors that may interact with Li via dative bonds are

illustrated in **Figure 1c**. The NBO analysis[32,33] identified one s-type lone pair, $n^{(\sigma)}$, for N atoms formed from a hybrid orbital that mixes 2s and 2p characters (29.9% s and 70.1% p), while two geometrically and energetically distinct lone pairs were found for O atoms: one s-type (59.4% s and 40.6% p) and the other p-type, $n^{(\pi)}$, consisting of 100% p character. It is worth noting that the lone pairs show some degree of delocalization over the aromatic rings, exhibiting partial electron occupancies ranging from 1.88 to 1.98 |e| due to the highly conjugated HATAQ system.

Single-crystal X-ray diffraction (SXRD) analysis of HATAQ revealed the unique molecular arrangement (**Figure 1b and S4**) not seen previously in organic small-molecule cathode materials. Suitable quality crystals were obtained by dissolving a small amount of HATAQ in hot dimethyl sulfoxide (DMSO) solvent and allowing the solution to slowly cool down to room temperature. The compound crystallizes in a trigonal space group (*R* -3 *c*, SI **Table S1**) in what can be described as a supramolecular analog of graphite. The interlayer space between the sheets of HATAQ molecules is filled with DMSO molecules, which are the solvent used during crystallization. The unique trigonal geometrical shape of HATAQ molecule and the presence of multiple weak hydrogen bond donor groups (C—H) and strong hydrogen bond acceptor groups (O) lead to a highly structured 2D arrangement seen in **Figure 1b**. In each HATAQ molecule, a total of six hydrogen atoms from the C—H bonds on the far ends of the molecule interact with a total of six oxygen atoms, two from each of the neighboring three HATAQ molecules. Each protruding diazaanthraquinone arm of one molecule perfectly fits inside a cleft formed in between two arms of the neighboring molecule via peculiar lock-key hydrogen bonding interactions.[34,35] This arrangement is repeated for every HATAQ molecule resulting in a supramolecular graphene-like 2D sheet structure. The distance between the hydrogen atom in C—H bond and the closest carbonyl oxygen atom from the adjacent molecule is quite long, 2.48 Å. Nevertheless, this bond length is less than 2.61 Å, which is the sum of the van der Waals radii for oxygen and hydrogen,[36] suggesting

that orbital overlap might still occur. To investigate whether relevant geometries enable these hydrogen bonds which are some of the longest found in nature, [37] we performed NBO analysis for the DFT optimized structure of HATAQ dimer. The results indicate that 2.02 kcal mol^{-1} is released by the mixing of the carbonyl $n^{(\sigma)}$ lone pair with the C—H σ* orbital (**Figure S16**). Although relatively weak, these hydrogen bonds could make a significant contribution to the stability of HATAQ 2D layer arrangement. Akin to the molecular forces governing protein folding, the high number of noncovalent interactions between the neighboring HATAQ molecules as well as synergistic interaction between 6 hydrogen bond donors and 6 hydrogen bond acceptors, essentially stitch the molecules together forming a stable supramolecular 2D polymer.[38]

2.2. Electrochemical Performance

Electrochemical performance of HATAQ as cathode material was tested in coin cells with Li metal as the counter electrode and 1 M lithium bis(trifluoromethanesulfonyl)imide (LiTFSI) in 1,3-dioxolane (DOL)/1,2-dimethoxyethane (DME) (1:2 v/v) with 0.3 wt% $LiNO_3$ as the electrolyte. **Figure 2a** shows the discharge (lithiation)/charge (delithiation) profiles of HATAQ at 200 mA g^{-1} (C/2.5, reaction with 12 Li in 2.5 h). During discharge, a short plateau is observed at 2.85 V vs. Li/Li^+, followed by a very short one at 2.18 V with a discharge capacity of 426 mAh g^{-1}. During charge, two plateaus can be observed at 2.30 and 3.05 V. These plateaus are consistent with the main peak positions in the cyclic voltammogram (CV) of the HATAQ in **Figure 2b**. The CV characteristics suggest that the compound has multiple reversible redox reactions during cell cycling.[28,39] The discharge/charge profiles of the compound at current densities of 400 and 800 mA g^{-1} are also given in **Figure 2a**. At a higher rate, the voltages of the plateaus decrease due to kinetic effects.[40] However, there is only a slight decrease in capacities with 416 and 379 mAh g^{-1} for 400 and 800 mA g^{-1}, respectively.

Figure 2c shows the capacity retention of the three current rates. It is apparent that the HATAQ coin cells have excellent capacity retention at these rates, delivering reversible capacities of 376, 373, and 367 mAh g^{-1} with a retention of 86.4, 88.9, and 94.8 % after 100 cycles for 200, 400, and 800 mA g^{-1}, respectively.

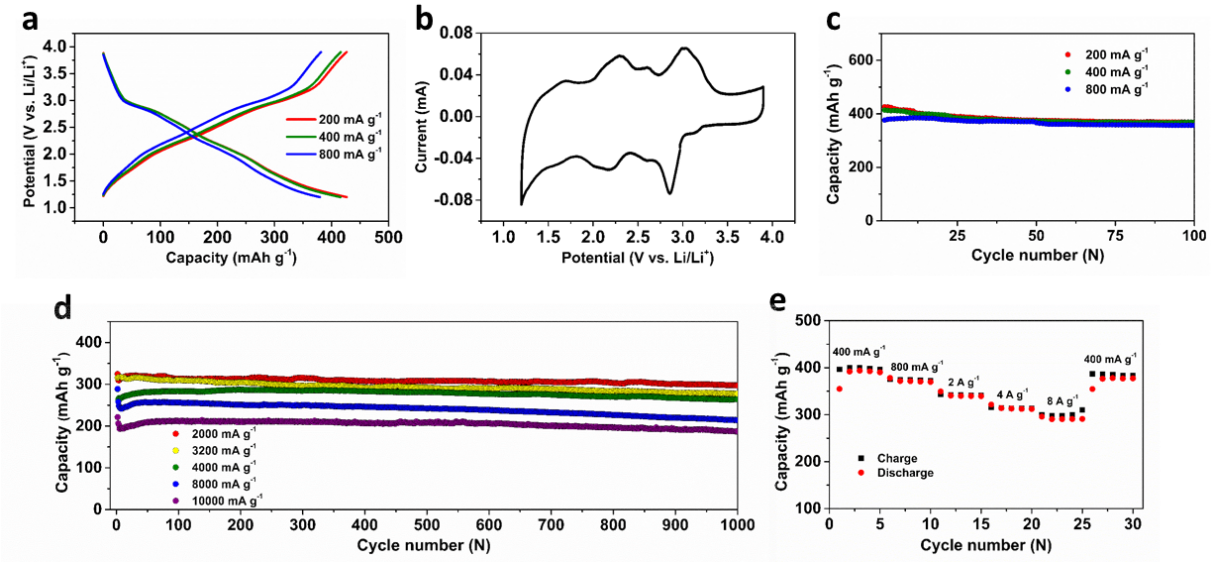

Figure 2. Electrochemical properties of HATAQ. (a, b, c) Voltage profiles of HATAQ electrodes at current densities ranging from 200 mA g^{-1} (0.4C) to 800 mA g^{-1} (1.6C) together with the cyclic voltammogram at a scan rate of 0.1 mV s^{-1} and capacity retention. (d, e) The capacity retention of HATAQ at high rates from 2 A g^{-1} (4C) to 10 A g^{-1} (19C) and rate capability at various current densities.

In addition to these relatively low rates, even higher current densities up to 10 A g^{-1} (~19C) were tested on HATAQ as shown in **Figure 2d**. It has been found that this redox-active molecule is remarkably stable for over 1000 cycles delivering reversible specific capacities of 310, 297, 285, 242, and 209 mAh g^{-1}, resulting in retention values of 91.6, 87.9, 91.5, 74.0, and 84.6 % for 2, 3.2, 4, 8, and 10 A g^{-1}, respectively. The electrochemical performance was also investigated in terms of the rate capabilities (**Figure 2e**). When the loading current is varied from 0.4 to 8 A g^{-1}, a highly reversible rate capability curve is obtained. Moreover, a capacity retention of 96.4 % was observed when the rate of 0.4 A g^{-1}

was reapplied to the cell. This is attributed to the facile charge transfer kinetics of the extended π-conjugated molecules and Li ions. The electrochemical performance with such high capacity and excellent rate capability as seen in HATAQ has rarely been observed in small-molecule-based organic batteries.[28]

The energy density of HATAQ has also been calculated. Based on the discharge capacity of 426 mAh g^{-1} at 200 mA g^{-1} (0.4C) and the average discharge potential of 2.1 V, the gravimetric energy density is estimated to 894 Wh kg^{-1} with respect to the cathode material or 298 Wh kg^{-1} with respect to the battery weight, when the mass of the electrode is normally considered to be approximately 1/3 of the total weight of the cell.[28] This energy density is found to be significantly higher than the value reported for 3Q which is ~250 Wh kg^{-1} (whole cell).[28] In addition, electronic conductivity of HATAQ is expected to improve compared to the parent compound due to extended aromatic structure and conjugation.[41] These results indicate that our design strategy to introduce conjugated electron-withdrawing quinone moieties to extend the π-conjugation and increase the number of redox active sites is highly effective at enhancing the specific capacity, cell voltage, charge transfer as well as cycling stability in organic electrolytes.

2.3. Lithiation Mechanism

To understand the underlying mechanism of the Li-ion storage in HATAQ, in-situ Raman spectroscopy was performed. **Figure 3** shows the Raman spectra at different discharge and charge states when HATAQ electrode was cycled at 200 mA g^{-1}. The bands at 1570 and 1665 cm^{-1} can be assigned to the C=N and C=O groups, respectively.[42–44] As the HATAQ is discharged from OCV to 1.2 V, it is clear that both the C=N and C=O bands become gradually weaker suggesting the interactions of the O and N atoms with the Li ions during the reduction. When the cell is recharged up to 3.9 V, the intensities of the two bands appear higher and become comparable to those seen at the pristine state, indicating a highly

reversible lithiation/delithiation process. **Figure S8** shows ex-situ Raman spectra of the electrodes with higher resolution confirming the same result for the redox activity of the two electroactive functional groups. A similar trend is seen in the Fourier-transform infrared (FT-IR) spectra. As shown in **Figure S9 and S10**, the FT-IR results of the HATAQ electrodes exhibit two distinct absorption peaks at 1687 and 1582 cm^{-1}, which can be assigned to the stretching vibration modes of carbonyl (C=O) and imine (C=N) groups, respectively.[42,45] The two characteristic peaks apparently weaken during discharge, coinciding with the coordination of Li ions with the redox active sites. Likewise, during the charge process, the C=O and C=N peaks reemerge further supporting highly reversible nature of the overall electrochemical cycle.

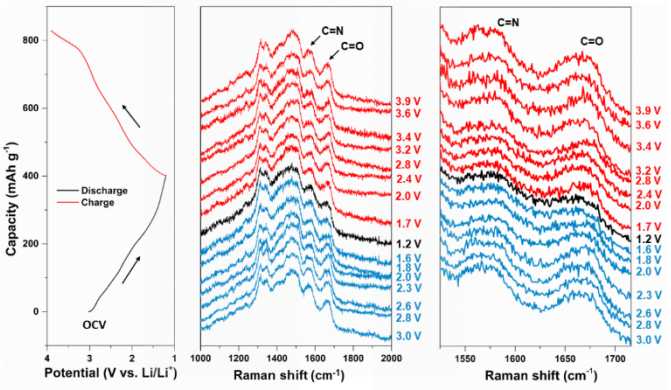

Figure 3. In-situ Raman spectra of HATAQ electrodes at different states of charge, together with the corresponding discharge and charge profile at 200 mA g^{-1} in the voltage range of 1.2-3.9 V, clearly indicating the changes of the redox centers in HATAQ, C=N and C=O, during cell cycling.

To further elucidate the redox mechanism during the lithiation/delithiation process, the ex-situ X-ray photoelectron spectroscopy (XPS) spectra were collected on the discharged and charged electrodes. As demonstrated in **Figure S12**, the C 1s spectrum of the pristine HATAQ electrode can be deconvoluted into five peaks, which are centered approximately at 284.7, 285.0, 286.3, 288.1, and 290.7 eV corresponding to C=C, C–C, C=N, C=O, and C-F, respectively.[42,45,46] The binding energy of C=N was found to be close to that of C=O in the

HATAQ molecule due to the lone pair electrons of the N and O atoms which are able to delocalize into the π-conjugated system as shown in our NBO analysis. As the cell is discharged from the pristine state down to 2.1 and 1.2 V, the two major peaks of C=N and C=O are gradually weakened, while two new peaks C–N (285.0 eV) and C–O (285.6 eV) emerge and become stronger, suggesting lithiation process at the two redox centers of HATAQ.[45,47] When the cell is charged back to 2.1 V, the C–N and C–O peaks appear weaker and become much smaller at 3.9 V, whereas the population of C=O and C=N increases as the cell potential increases. The O 1s XPS spectra (**Figure S12**) also indicate a similar phenomenon during cell cycling. The HATAQ in the pristine state shows the C=O peak (532.1 eV) which becomes smaller during discharge, while C–O (532.6 eV) emerges when the compound is discharged to 2.1 and 1.2 V.[46,48] This behavior is found to be almost entirely reversible during charge. The incomplete transformation of C–O to C=O may be due to the kinetic limitations in the solid-state electrochemical reaction.

In addition, the involvement of the HATAQ N atoms in coordination with Li during the redox reaction is confirmed by the N 1s XPS results as shown in **Figure S12**. The pristine electrode exhibits a C=N peak at 400.0 eV which appears to be smaller as the redox-active molecule HATAQ undergoes a reduction reaction in the presence of Li ions (**Figure S12**, discharge spectra).[49,50] At the same time, two new peaks appear at 400.6 and 398.5 eV which correspond to C–N and N–Li, respectively.[49–52] During the charge process, a reverse trend can be observed, with C=N peak growing stronger as well as C–N and N–Li becoming weaker.

The results from XPS, the Raman, and FT-IR spectra are all in a good agreement, strongly suggesting the highly reversible nature of the HATAQ redox activity with Li. Based on these mechanistic studies, it is clear that both carbonyl and imine groups of HATAQ are redox-active and both groups can interact with Li ions during discharge/charge processes. This may well be explained by the very small difference in the atomic charges and electronegativity

between O and N atoms in the extended π-conjugated HATAQ structure (**Figure 1a**). Furthermore, our NBO analysis for a singly lithiated HATAQ molecule (HATAQ-Li) indicates almost equal contribution of N and O lone pairs to the Li binding (**Figure S17**).

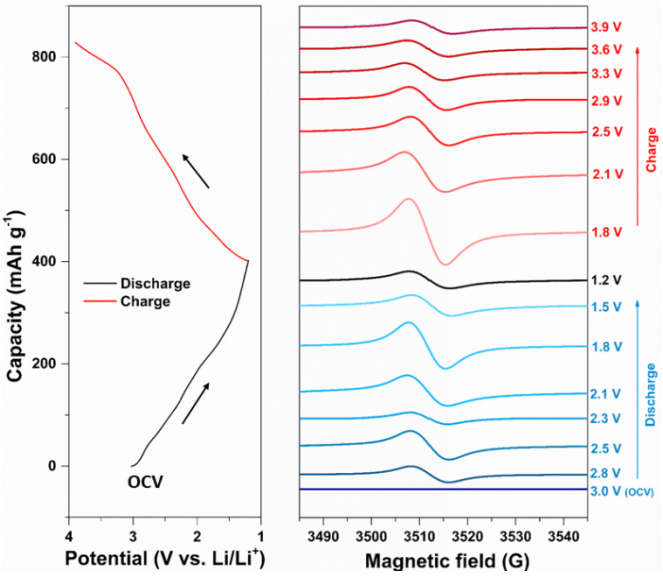

Figure 4. Ex-situ EPR spectra of the HATAQ electrodes during discharge and charge.

To gain additional insight into the Li storage mechanism of HATAQ, ex-situ electron paramagnetic resonance (EPR) spectroscopy study was performed to investigate the evolution of the electronic structure during the cell cycling. As illustrated in **Figure 4**, starting from OCV (3.0 V), the pristine HATAQ shows negative EPR signal, indicating no radical species present in HATAQ molecule. Once the discharge process is initiated, the EPR signal becomes stronger until it reaches 2.5 V, implying radical species being generated. The signal then dissipates and gets strongest at 1.8 V, followed by a decrease down to 1.2 V which is the cell cutoff voltage. The increase in EPR signal intensity can be ascribed to the increase of radical species concentration, which presumably corresponds to the transformations of the carbonyl and imine groups due to the interaction with Li ions and the acceptance of electrons.[53,54] As the potential rises during charge, the EPR signal becomes strongest at 1.8 V and gradually

decreases with increasing potential up to 3.9 V. To locate the delocalization of the unpaired electron in the HATAQ-Li complexes with an odd number of Li ions (doublet state), we performed the Mulliken spin density calculations. The results show that the spin densities are primarily delocalized over O and N atoms participating in Li chelation with some spin density residing on the aromatic rings due to π-conjugation (**Figure S18**). The simultaneous spin distribution over carbonyl and imine groups further confirms their active role in the interactions with Li ions during charge/discharge processes.

The structural stability of the HATAQ material was investigated by powder X-ray diffraction (PXRD, **Figure S13**). The PXRD data of the solvent-free HATAQ, obtained by heating in vacuum at 120 °C, match well with the simulated PXRD pattern of the DFT optimized HATAQ structure. Ex-situ PXRD experiments were also conducted on the HATAQ electrodes at different states during cycling. As shown in **Figure S13**, when HATAQ is discharged down to 1.2 V and charged up to 3.9 V, the peak at ~27° corresponding to diffraction from the (006) plane remains visible suggesting that during lithiation process, the HATAQ is still crystalline with π-stacking being intact. This indicates that the 2D layered structure of HATAQ is stable throughout the lithiation/delithiation processes likely due to the in-plane supramolecular interactions, thus enhancing the cycling stability of HATAQ cathode. Additionally, ab initio molecular dynamics (MD) simulations at elevated temperature (127 °C) show similar 2D stacking in the initial and final structure (**Figure S19**), confirming the exceptional stability of the HATAQ supramolecular arrangement.

To further shed light on the HATAQ structural evolution during the lithiation process, we performed DFT calculations of the reduced HATAQ molecule in its corresponding lithiated states. Potentially, a single HATAQ molecule is capable of accepting of up to 12 Li ions and 12 electrons, which makes it, to the best of our knowledge, one of the only few examples of small-molecule organic cathode materials capable of accepting more than 10 electrons.[55,56] The global minimum structures of HATAQ–*n*Li (*n* = 1, 2, 3, 4, 5, 6, 7, 8, 9, 10, 11, 12) are

shown in **Figure S20**. According to our results in **Figure 5a**, electrochemical reduction of HATAQ with Li can be formally divided into two distinct processes: a formal reduction of quinone moieties is taking place upon reduction with up to 6 Li (n = 1—6); and further reduction of hexaazatriphenylene core with Li (n = 7—12). The first three lithiation steps lead to the formation of HATAQ–3Li, where each lithium forms a 5-membered chelate with one oxygen and one nitrogen atom within different clefts in the HATAQ molecule (**Figure 5b**).

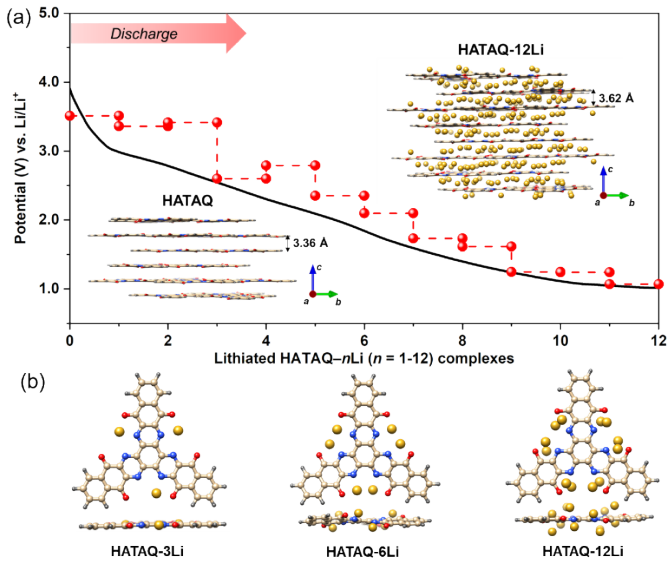

Figure 5. HATAQ lithiation steps obtained from DFT simulations. (a) Comparison of the calculated redox potentials (dotted red lines) with the experimental discharge curve (black solid line). Inset shows the DFT optimized periodic structures of the pristine and fully lithiated HATAQ. (b) Top and side views of the representative HATAQ-nLi (n = 3, 6, 12) complexes.

The energies of these three redox processes are within 0.17 V establishing the first plateau. The next lithiation step results in the HATAQ–4Li complex, in which 2 Li ions are sharing the same cleft (**Figure S20**). This leads to a significant decrease in the redox potential of 0.82 V, which is caused by ~20% drop in the Li binding energy (**Table S2**). Consequent two lithiation processes form the D_3-symmetric HATAQ–6Li structure, where every cleft accommodates 2 Li ions in a 5-membered chelate arrangement (**Figure 5b**). Therefore, at least two main redox potential levels related to the two-step three-electron transfer mechanism

can be established in agreement with the experimental discharge profile and the CV curve in **Figure 2a**. Next lithiation step leads to HATAQ–7Li, where the formation of the first oxygen-nitrogen chelate that is shared between 2 Li ions results in further decrease in the redox potential. Subsequent two lithiation processes follow the same pattern as before by forming HATAQ–9Li, where 3 Li ions are accommodated by each of the three HATAQ clefts. The final three lithiation processes lead to the formation of the highly symmetric HATAQ–12Li structure, which is prototypical to the HATAQ–6Li complex, but with 6 oxygen-nitrogen chelates sharing 6 pairs of Li ions. Notably, the HATAQ scaffold in the fully lithiated HATAQ–12Li complex is almost completely planar, suggesting that Li intercalation should not significantly perturb the 2D supramolecular arrangement in the synthesized HATAQ material. The periodic DFT calculations indeed confirm that Li ions readily intercalate between the HATAQ layers as shown in **Figure 5a**. Interestingly, this leads to only marginal volumetric expansion (~18%) in the fully lithiated structure, similar to that observed in graphite upon lithium intercalation (~13%).[57] Hence, the small volume expansion of HATAQ during lithiation might be responsible for the high cycling stability as was demonstrated in our electrochemical studies.

3. Conclusions

We have demonstrated the molecular design of small electroactive molecule HATAQ that organizes into a 2D supramolecular polymer via a unique network of unconventional lock-and-key hydrogen bonds in the solid state. The fine-tuning of the redox potential of this organic cathode material is further accomplished by manipulating its HOMO and LUMO energy levels. By introducing quinone moieties into the HATA molecule, the conjugation of the resulting HATAQ is thus extended, allowing electrons to delocalize through the π–π orbital interactions by resonance effect. As a consequence, the LUMO energy level of the molecule is lowered with higher electron affinity. The presence of the electron-withdrawing carbonyl groups in HATAQ also helps lower the LUMO level, thus leading to higher

reduction potential (~2.9 V vs Li/Li^+ compared to ~2.4 V for 3Q).[28,58] The HOMO–LUMO gap is reduced due to the extended π-electron orbital overlap in the conjugated system of HATAQ. This primarily leads to better electronic mobility, redox reversibility, and excellent rate capability as observed in HATAQ electrodes.[58,59] Moreover, the discharge product becomes more stabilized as the conjugation increases due to the resonance effect. Therefore, the possibilities of side reactions of the compound in the battery system are to be reduced, leading to superior cycle life.[59] Additionally, nitrogen and oxygen atoms form a near ideal arrangement that facilitates 5-membered chelate formation with Li ions during charge. Our computational analysis clearly shows that every fourth lithiation process (i.e. HATAQ–3Li/HATAQ–4Li, HATAQ–6Li/HATAQ–7Li, and HATAQ–9Li/HATAQ–10Li) is accompanied by a decrease in redox energy due to the introduction of shared Li ions, whether within the same cleft or same chelate. We thus conjecture that further increase in the number of appropriately positioned chelating groups could mitigate this behavior and potentially lead to small-molecule organic electroactive materials with significantly enhanced redox potential and superior discharge profile. Our molecular design strategy combined with mechanistic and structural insights is expected to result in many more members being added to the family of high-performance small-molecule-based organic cathode materials with markedly improved properties and electrochemical performance.

4. Experimental Section/Methods

HATAQ Synthesis

2,3-Diamino-1,4-naphtaquinone (61.2 g, 325 mmol) was dissolved in degassed glacial acetic acid (1500 mL). To this solution, cyclohexane hexaketone as an octahydrate (31.2 g, 100 mmol) was added in one portion. The reaction mixture was heated at reflux at 120 °C over 24 h period under the argon atmosphere. Upon reaction completion, the reaction mixture was cooled to 60 °C and the solid residue was recovered by filtration. The obtained dark brown

solid was successively washed with fresh glacial acetic acid (200 mL), ethanol (200 mL), acetone (200 mL), and water (4 x 250 mL), and dried under vacuum over 24 h. The resulting black solid was suspended in 25 % nitric acid (250 mL). The obtained suspension was heated at reflux with vigorous stirring at 100 °C for 2 h. The color of suspension turned from dark brown to dark orange upon heating. The reaction mixture was cooled to room temperature and the solid was separated by filtration on glass filter. Filter cake was washed with deionized water (5 x 500 mL) followed by drying under dynamic vacuum overnight. Title product was obtained as a yellow-orange powder (54.3 g, 87% yield). ^{1}H NMR (500 MHz, TFA-*d*, δ): 8.73-8.65 (m, 6H), 8.20-8.10 (m, 6H); HRMS (+ mode) *m/z*: $[M+H]^+$ calcd for $C_{36}H_{12}N_6O_6$, 625.0891; found, 625.0878.

Characterization

PXRD patterns were collected on Bruker D8 Advance ECO. Single-crystal X-ray diffraction experiments were performed by using Bruker D8 Venture dual X-ray single crystal diffractometer. XPS measurements were performed on ULVAC PHI 5000 VersaProbe Ⅲ with Al Kα (1487 eV) as an X-ray source. Survey scans were collected with a pass energy of 100 eV, followed by high-resolution scans of the C 1s, N 1s, and O 1s regions with a pass energy of 20 eV. All spectra were charge-corrected relative to the C 1s component at 284.5 eV binding energy and analyzed using CasaXPS software. The Raman spectra of the samples were collected by UniDRON Raman microscope with an excitation laser beam wavelength of 633 nm. FT-IR spectra were recorded on Nicolet iS5 or Nicolet 6700, Thermo Scientific. Scanning Electron Microscopy (SEM) images were collected on a SU8010 HR-FESEM scanning electron microscope. The EPR spectra were recorded on a Bruker EMX System EPR with X-band EPR spectrometer operating at 9.80 GHz. Microwave power was set to 2.002 mW. Sweep width was performed with 100G and a center field of 3510G. The field modulation frequency was set to 100 kHz, and the modulation amplitude was 6G. TGA was performed using TA Q50 instrument. High resolution mass spectrometric (HRMS) analysis

results were acquired by the University of Texas at Austin Mass Spectrometry Facility. The ^{1}H NMR spectrum was recorded on a Bruker AV-500.

Electrochemical Measurements

HATAQ was mixed and ground with Ketjen black conductive carbon and polyvinylidene fluoride (PVDF) in a 3:6:1 weight ratio. The mixture was then stirred in *N*-methyl-2-pyrrolidinone (NMP) and coated onto carbon paper which was used as current collector. The electrodes were dried overnight at 80 °C in vacuum. CR2032 coin cells were assembled by using Li metal as anode, 1 M LiTFSI in 1:2 v/v DOL/DME with 0.3 wt% $LiNO_3$ as electrolyte, and Whatman glass microfiber (GF/A) membrane as separator. Cell fabrication was done in argon-filled glovebox with O_2 and H_2O levels below 0.3 ppm. The galvanostatic charge/discharge and cyclic voltammetry measurements were carried out with a Neware battery cycler and BCS-805 system (BioLogic).

Density Functional Theory Calculations

Electronic structure calculations of the HATAQ molecule and the respective lithiated complexes were performed with the Gaussian 09 D.01 software.[60] We adopted the DFT approach for our calculations using the B3LYP density functional with the 6-31+G(d,p) basis set. Frequency calculations were performed at the B3LYP/6-31+G(d) level to ensure that geometries (optimized at the same level of theory) were minima and to compute zero-point energies and thermal corrections (T = 298.15 K) to Gibbs free energy. DME solvent was chosen in the polarizable continuum model using the integral equation formalism variant (IEFPCM) with the solvent paraments taken from C. Peng et al.[28] in order to provide a fair comparison of the predicted HOMO-LUMO gaps and redox potentials for the 3Q[28] and HATAQ molecules. In particular, the static dielectric constant (ε) was set to 7.20, the molecular radius of the solvent: 2.78255 Å, the density of the solvent: 0.005804 particles/Å, and the molar volume of the solvent: 103.7911 cm^{-3}. The redox calculations require the global minimum geometries for each lithiated HATAQ species. We performed an unbiased

quantum-chemical search for the most energetically stable HATAQ-Li complexes using the Coalescence Kick (CK) program,[61] which was successfully used previously to predict the global minimum structures of lithiated phosphorus clusters.[62] Briefly, the initial geometry of the HATAQ molecular unit and the desired number of Li atoms were specified in the input file. The CK generated ~200 random structures possessing reasonable connectivity: the two units of the complex (HATAQ and Li species) are considered as connected in a fragment if the distances between them are less than the sum of the corresponding van der Waals radii. The generated structures were optimized at the B3LYP/3-21G level of theory and then ten low-lying isomers found by this method were reoptimized using the 6-31+G(d,p) basis set to establish the global minimum configuration for a given stoichiometry. The reduction potential of redox active HATAQ molecule in the solution was calculated using the formula:

$$E^{redox} = -(G^{final} - G^{initial} - G^{Li})/nF$$

where G^{final}, $G^{initial}$, and G^{Li} are the calculated Gibbs free energies (kcal mol^{-1}) of the final and initial lithiated states of the HATAQ molecule, and Li atom, respectively; n is the number of electrons transferred in the process and F is the Faraday constant.

Chemical bonding analysis was performed using the NBO methodology.[32] The donor-acceptor interaction energy (second-order stabilization energies, $E^{(2)}$) in the NBOs was estimated via second-order perturbation theory analysis of the Fock matrix.[28]

Periodic DFT calculations were performed using the Vienna Ab-initio Simulation Package (VASP).[63–66] The valence electronic states were expanded in a basis of plane waves, while the core valence interactions were described using the Projector Augmented Wave (PAW) approach.[67,68] The plane wave kinetic energy cutoff was set to 600 eV and the PBE GGA functional[69] was employed to describe the exchange correlation interactions. The DFT-D3 approach of Grimme with zero damping[70] was used to account for the van der Waals interactions. Cell optimizations of the HATAQ structure with DMSO solvent were carried out starting from the single-crystal X-ray diffraction structure (see **Table S3** for the full

comparison of the DFT optimized lattice parameters and experimental data), while the solvent free HATAQ structure was obtained by geometry optimization after removal of DMSO molecules, from the experimental crystal structure. The SCF convergence threshold was set to 10^{-5} eV and a Pulay scheme[71] was used for charge density mixing during the SCF solution. Molecular dynamics (MD) simulations in VASP utilized a plane wave energy cutoff of 500 eV, and the Brillouin zone was sampled using the Gamma point approximation. An MD time step of 1 fs was used, and the temperature (400 K) was controlled using the Nose–Hoover thermostat. The MD simulations lasted for a duration of 2 ps (2000 time steps in total).

Author Contributions

M.-S. W. performed all the electrochemical studies, with intellectual input from T.-H. C., I. P., X.-G. S., and W. K. H. L. and I. P. synthesized the compound HATAQ with input from T.-H. C., S. D., and W. K. A. S. I. designed, performed, and analyzed the theoretical studies. H. L. performed TGA analysis. D.-W. H. performed the crystallization of HATAQ. J.-C. L. conducted the XPS experiments. The interpretation of experiments was done by T.-H. C. and W. K. T.-H. C., A. S. I., I. P., and W. K. designed the study and wrote the manuscript, incorporating the input from all other authors.

Conflicts of Interest

Provisional patent related to this research, entitled ‘Cathode Material of Lithium-ion Battery and Fabricating Method Thereof, and Lithium-ion Battery’, has been filed by the T.-H. C., W. K., and National Cheng Kung University. Taiwan Application No. 109139414, filed on 11 November 2020.

[CCDC 1996183 contains the supplementary crystallographic data for this paper. These data can be obtained free of charge from The Cambridge Crystallographic Data Centre via www.ccdc.cam.ac.uk/data_request/cif.]

Supporting Information
Supporting Information is available from the Wiley Online Library or from the author.

Acknowledgements
This work was supported by the Ministry of Science and Technology of Taiwan under grant MOST108-2113-M-006-016 (to T.-H. C.) and the Young Scholar Fellowship Program MOST108-2636-E-006-001 (to W. K.). This work was also financially supported by the Hierarchical Green-Energy Materials (Hi-GEM) Research Center, from the Featured Areas Research Center Program within the framework of the Higher Education Sprout Project by the Ministry of Education (MOE) and the Ministry of Science and Technology (MOST 109-2634-F-006-020) in Taiwan (to W. K.). This research was supported in part by High Education Sprout Project, Ministry of Education of the Headquarters of University Advancement at National Cheng Kung University (to T.-H. C. and W. K.). The research of H. L., X.-G. S., S. D., A. S. I., and I. P. was supported by the U.S. Department of Energy, Office of Science, Office of Basic Energy Sciences, Materials Sciences and Engineering Division under contract number DE-AC05-00OR22725. This research used resources of the Computer and Data Environment for Science (CADES) at Oak Ridge National Laboratory, managed by UT-Battelle, LLC for the U.S. DOE under Contract DE-AC05-00OR22725. The authors are indebted to Dr. Ting-Shen Kuo (National Taiwan Normal University) for the collection and the refinement of crystallographic data. Authors thank the University of Texas at Austin Mass Spectrometry Facility staff for acquiring high resolution mass spectra.

Received: ((will be filled in by the editorial staff))
Revised: ((will be filled in by the editorial staff))
Published online: ((will be filled in by the editorial staff))

References

[1] M. Armand, J.-M. Tarascon, *Nature* **2008**, *451*, 652–657.

[2] Y. Lu, J. Chen, *Nat. Rev. Chem.* **2020**, *4*, 127–142.

[3] K. Qin, J. Huang, K. Holguin, C. Luo, *Energy Environ. Sci.* **2020**, *13*, 3950–3992.

[4] P. Poizot, J. Gaubicher, S. Renault, L. Dubois, Y. Liang, Y. Yao, *Chem. Rev.* **2020**, *120*, 6490–6557.

[5] M. Lee, J. Hong, J. Lopez, Y. Sun, D. Feng, K. Lim, W. C. Chueh, M. F. Toney, Y. Cui, Z. Bao, *Nat. Energy* **2017**, *2*, 861–868.

[6] Y. Liang, Y. Yao, *Joule* **2018**, *2*, 1690–1706.

[7] H. Lyu, J. Liu, S. Mahurin, S. Dai, Z. Guo, X.-G. Sun, *J. Mater. Chem. A* **2017**, *5*, 24083–24090.

[8] H. Lyu, P. Li, J. Liu, S. Mahurin, J. Chen, D. K. Hensley, G. M. Veith, Z. Guo, S. Dai, X.-G. Sun, *ChemSusChem* **2018**, *11*, 763–772.

[9] C. Han, H. Li, R. Shi, T. Zhang, J. Tong, J. Li, B. Li, *J. Mater. Chem. A* **2019**, *7*, 23378–23415.

[10] J. Yang, P. Xiong, Y. Shi, P. Sun, Z. Wang, Z. Chen, Y. Xu, *Adv. Funct. Mater.* **2020**, *30*, 1909597.

[11] X. Yang, Y. Hu, N. Dunlap, X. Wang, S. Huang, Z. Su, S. Sharma, Y. Jin, F. Huang, X. Wang, S. Lee, W. Zhang, *Angew. Chem. Int. Ed.* **2020**, *59*, 20385–20389.

[12] K. Shinozaki, Y. Tomizuka, A. Nojiri, *Jpn. J. Appl. Phys.* **1984**, *23*, L892–L894.

[13] L. Bugnon, C. J. H. Morton, P. Novak, J. Vetter, P. Nesvadba, *Chem. Mater.* **2007**, *19*, 2910–2914.

[14] K. Oyaizu, T. Kawamoto, T. Suga, H. Nishide, *Macromolecules* **2010**, *43*, 10382–10389.

[15] W. Guo, Y.-X. Yin, S. Xin, Y.-G. Guo, L.-J. Wan, *Energy Environ. Sci.* **2012**, *5*, 5221–5225.

[16] W. J. Chung, J. J. Griebel, E. T. Kim, H. Yoon, A. G. Simmonds, H. J. Ji, P. T. Dirlam, R. S. Glass, J. J. Wie, N. A. Nguyen, B. W. Guralnick, J. Park, Á. Somogyi, P. Theato, M. E. Mackay, Y.-E. Sung, K. Char, J. Pyun, *Nat. Chem.* **2013**, *5*, 518–524.

[17] S. H. Je, H. J. Kim, J. Kim, J. W. Choi, A. Coskun, *Adv. Funct. Mater.* **2017**, *27*, 1703947.

[18] Z. Shadike, H.-S. Lee, C. Tian, K. Sun, L. Song, E. Hu, I. Waluyo, A. Hunt, S. Ghose, Y. Hu, J. Zhou, J. Wang, P. Northrup, S.-M. Bak, X.-Q. Yang, *Adv. Energy Mater.* **2019**, *9*, 1900705.

[19] J. Kim, A. Elabd, S.-Y. Chung, A. Coskun, J. W. Choi, *Chem. Mater.* **2020**, *32*, 4185–4193.

[20] Y. Hanyu, T. Sugimoto, Y. Ganbe, A. Masuda, I. Honma, *J. Electrochem. Soc.* **2013**, *161*, A6.

[21] T. Matsunaga, T. Kubota, T. Sugimoto, M. Satoh, *Chem. Lett.* **2011**, *40*, 750–752.

[22] Z. Yang, T. Wang, H. Chen, X. Suo, P. Halstenberg, H. Lyu, W. Jiang, S. M. Mahurin, I. Popovs, S. Dai, *ACS Energy Lett.* **2020**, 41–51.

[23] S. Lee, G. Kwon, K. Ku, K. Yoon, S.-K. Jung, H.-D. Lim, K. Kang, *Adv. Mater.* **2018**, *30*, 1704682.

[24] M. Kolek, F. Otteny, P. Schmidt, C. Mück-Lichtenfeld, C. Einholz, J. Becking, E. Schleicher, M. Winter, P. Bieker, B. Esser, *Energy Environ. Sci.* **2017**, *10*, 2334–2341.

[25] H. Lyu, C. J. Jafta, I. Popovs, H. M. Meyer, J. A. Hachtel, J. Huang, B. G. Sumpter, S. Dai, X.-G. Sun, *J. Mater. Chem. A* **2019**, *7*, 17888–17895.

[26] A. Jouhara, N. Dupré, A.-C. Gaillot, D. Guyomard, F. Dolhem, P. Poizot, *Nat. Commun.* **2018**, *9*, 4401.

[27] K. Nakashima, T. Shimizu, Y. Kamakura, A. Hinokimoto, Y. Kitagawa, H. Yoshikawa, D. Tanaka, *Chem. Sci.* **2019**, *11*, 37–43.

[28] C. Peng, G.-H. Ning, J. Su, G. Zhong, W. Tang, B. Tian, C. Su, D. Yu, L. Zu, J. Yang, M.-F. Ng, Y.-S. Hu, Y. Yang, M. Armand, K. P. Loh, *Nat. Energy* **2017**, *2*, 17074.

[29] J. L. Segura, R. Juárez, M. Ramos, C. Seoane, *Chem. Soc. Rev.* **2015**, *44*, 6850–6885.

[30] Z. Zhao, Y. Xiao, Y. Zhang, H. Wang, *RSC Adv.* **2013**, *3*, 21373–21376.

[31] R. Juárez, M. M. Oliva, M. Ramos, J. L. Segura, C. Alemán, F. Rodríguez-Ropero, D. Curcó, F. Montilla, V. Coropceanu, J. L. Brédas, Y. Qi, A. Kahn, M. C. Ruiz Delgado, J. Casado, J. T. López Navarrete, *Chem. – Eur. J.* **2011**, *17*, 10312–10322.

[32] J. P. Foster, F. Weinhold, *J. Am. Chem. Soc.* **1980**, *102*, 7211–7218.

[33] A. E. Reed, L. A. Curtiss, F. Weinhold, *Chem. Rev.* **1988**, *88*, 899–926.

[34] Q. Tang, Z. Liang, J. Liu, J. Xu, Q. Miao, *Chem. Commun.* **2010**, *46*, 2977–2979.

[35] Z. Liang, Q. Tang, J. Liu, J. Li, F. Yan, Q. Miao, *Chem. Mater.* **2010**, *22*, 6438–6443.

[36] R. S. Rowland, R. Taylor, *J. Phys. Chem.* **1996**, *100*, 7384–7391.

[37] S. Horowitz, R. C. Trievel, *J. Biol. Chem.* **2012**, *287*, 41576–41582.

[38] L. Jiang, L. Lai, *J. Biol. Chem.* **2002**, *277*, 37732–37740.

[39] C.-H. Chang, A.-C. Li, I. Popovs, W. Kaveevivitchai, J.-L. Chen, K.-C. Chou, T.-S. Kuo, T.-H. Chen, *J. Mater. Chem. A* **2019**, *7*, 23770–23774.

[40] W. Kaveevivitchai, A. Huq, A. Manthiram, *J. Mater. Chem. A* **2017**, *5*, 2309–2318.

[41] B. An, K. Wen, S. Feng, X. Pan, W. Wu, X. Guo, J. Zhang, *J. Comput. Chem.* **2018**, *39*, 773–779.

[42] Z. Lei, Q. Yang, Y. Xu, S. Guo, W. Sun, H. Liu, L.-P. Lv, Y. Zhang, Y. Wang, *Nat. Commun.* **2018**, *9*, 576.

[43] B. Zhuang, M. Fujitsuka, S. Tojo, D. W. Cho, J. Choi, T. Majima, *J. Phys. Chem. A* **2018**, *122*, 8738–8744.

[44] Y. Zhu, P. Chen, Y. Zhou, W. Nie, Y. Xu, *Electrochimica Acta* **2019**, *318*, 262–271.

[45] R. Shi, L. Liu, Y. Lu, C. Wang, Y. Li, L. Li, Z. Yan, J. Chen, *Nat. Commun.* **2020**, *11*, 178.

[46] Q. Xue, D. Li, Y. Huang, X. Zhang, Y. Ye, E. Fan, L. Li, F. Wu, R. Chen, *J. Mater. Chem. A* **2018**, *6*, 12559–12564.

[47] R. Guo, Y. Wang, S. Heng, G. Zhu, V. S. Battaglia, H. Zheng, *J. Power Sources* **2019**, *436*, 226848.

[48] K. W. Nam, H. Kim, Y. Beldjoudi, T. Kwon, D. J. Kim, J. F. Stoddart, *J. Am. Chem. Soc.* **2020**, *142*, 2541–2548.

[49] Z. Man, P. Li, D. Zhou, R. Zang, S. Wang, P. Li, S. Liu, X. Li, Y. Wu, X. Liang, G. Wang, *J. Mater. Chem. A* **2019**, *7*, 2368–2375.

[50] M. Mao, C. Luo, T. P. Pollard, S. Hou, T. Gao, X. Fan, C. Cui, J. Yue, Y. Tong, G. Yang, T. Deng, M. Zhang, J. Ma, L. Suo, O. Borodin, C. Wang, *Angew. Chem. Int. Ed.* **2019**, *58*, 17820–17826.

[51] J. Hong, M. Lee, B. Lee, D.-H. Seo, C. B. Park, K. Kang, *Nat. Commun.* **2014**, *5*, 5335.

[52] M. Lee, J. Hong, D.-H. Seo, D. H. Nam, K. T. Nam, K. Kang, C. B. Park, *Angew. Chem. Int. Ed.* **2013**, *52*, 8322–8328.

[53] S. Gu, S. Wu, L. Cao, M. Li, N. Qin, J. Zhu, Z. Wang, Y. Li, Z. Li, J. Chen, Z. Lu, *J. Am. Chem. Soc.* **2019**, *141*, 9623–9628.

[54] Q. Jiang, P. Xiong, J. Liu, Z. Xie, Q. Wang, X.-Q. Yang, E. Hu, Y. Cao, J. Sun, Y. Xu, L. Chen, *Angew. Chem. Int. Ed.* **2020**, *59*, 5273–5277.

[55] M. Pasquali, G. Pistoia, T. Boschi, P. Tagliatesta, *Solid State Ion.* **1987**, *23*, 261–266.

[56] W. Huang, S. Zheng, X. Zhang, W. Zhou, W. Xiong, J. Chen, *Energy Storage Mater.* **2020**, *26*, 465–471.

[57] S. Schweidler, L. de Biasi, A. Schiele, P. Hartmann, T. Brezesinski, J. Janek, *J. Phys. Chem. C* **2018**, *122*, 8829–8835.

[58] H. Banda, D. Damien, K. Nagarajan, A. Raj, M. Hariharan, M. M. Shaijumon, *Adv. Energy Mater.* **2017**, *7*, 1701316.

[59] H. Lyu, X.-G. Sun, S. Dai, *Adv. Energy Sustain. Res.* **2021**, *2*, 2000044.

[60] G. W. T. M. J. Frisch, H. B. Schlegel, G. E. Scuseria, M. A. Robb, J. R. Cheeseman, G. Scalmani, V. Barone, B. Mennucci, G. A. Petersson, H. Nakatsuji, M. Caricato, X. Li, H. P. Hratchian, A. F. Izmaylov, J. Bloino, G. Zheng, J. L. Sonnenberg, M. Hada, M. Ehara, K. Toyota, R. Fukuda, J. Hasegawa, M. Ishida, T. Nakajima, Y. Honda, O. Kitao, H. Nakai, T. Vreven, J. A. Montgomery, Jr., J. E. Peralta, F. Ogliaro, M. Bearpark, J. J. Heyd, E. Brothers, K. N. Kudin, V. N. Staroverov, R. Kobayashi, J. Normand, K. Raghavachari, A. Rendell, J. C. Burant, S. S. Iyengar, J. Tomasi, M. Cossi, N. Rega, J. M. Millam, M. Klene, J. E. Knox, J. B. Cross, V. Bakken, C. Adamo, J. Jaramillo, R. Gomperts, R. E. Stratmann, O. Yazyev, A. J. Austin, R. Cammi, C. Pomelli, J. W. Ochterski, R. L. Martin, K. Morokuma, V. G. Zakrzewski, G. A. Voth, P. Salvador, J. J. Dannenberg, S. Dapprich, A. D. Daniels, Ö. Farkas,

J. B. Foresman, J. V. Ortiz, J. Cioslowski and D. J. Fox, *Gaussian 9 (Revision D.01) Gaussian*, Gaussian, Inc., Wallingford, CT, 2009

[61] A. P. Sergeeva, B. B. Averkiev, H.-J. Zhai, A. I. Boldyrev, L.-S. Wang, *J. Chem. Phys.* **2011**, *134*, 224304.

[62] A. S. Ivanov, A. J. Morris, K. V. Bozhenko, C. J. Pickard, A. I. Boldyrev, *Angew. Chem. Int. Ed.* **2012**, *51*, 8330–8333.

[63] G. Kresse, J. Hafner, *Phys. Rev. B* **1993**, *47*, 558–561.

[64] G. Kresse, J. Hafner, *Phys. Rev. B* **1994**, *49*, 14251–14269.

[65] G. Kresse, J. Furthmüller, *Phys. Rev. B* **1996**, *54*, 11169–11186.

[66] G. Kresse, J. Furthmüller, *Comput. Mater. Sci.* **1996**, *6*, 15–50.

[67] P. E. Blöchl, *Phys. Rev. B* **1994**, *50*, 17953–17979.

[68] G. Kresse, D. Joubert, *Phys. Rev. B* **1999**, *59*, 1758–1775.

[69] J. P. Perdew, K. Burke, M. Ernzerhof, *Phys. Rev. Lett.* **1996**, *77*, 3865–3868.

[70] Stefan Grimme, Jens Antony, Stephan Ehrlich, Helge Krieg, *J. Chem. Phys.* **2010**, *132*, 154104.

[71] P. Pulay, *Chem. Phys. Lett.* **1980**, *73*, 393–398.

Table of Contents

To transition into a low carbon society, organic rechargeable batteries are a preferred alternative to the metal-based inorganic counterparts. A comprehensive strategy on the molecular design of an organic small-molecule-based cathode is revealed. This well-engineered material is able to overcome the common issues found in organic electrodes with unparalleled electrochemical performance, ranked among the best organic molecules for Li-ion batteries.

M.-S. Wu, T.-H. Chen, H. Lyu, T.-W. Huang, S. Dai, X.-G. Sun, A. S. Ivanov, J.-C. Lee, I. Popovs,* W. Kaveevivitchai*

Supramolecular Self-Assembled Multi-Electron-Acceptor Organic Molecule as High-Performance Cathode Material for Li-Ion Batteries

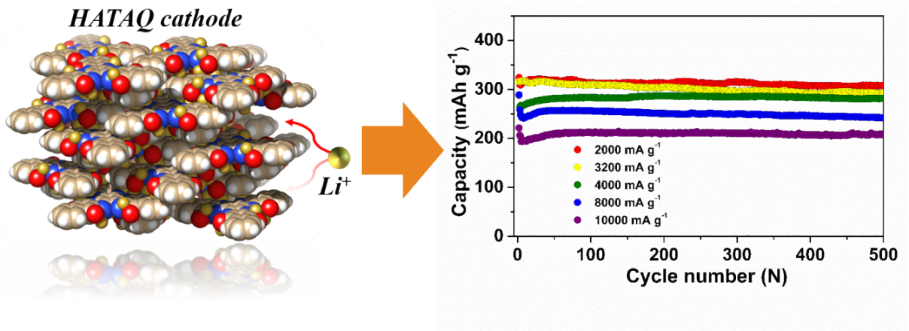

ToC figure ((110 mm broad × 20 mm high.))

Supporting Information

Supramolecular Self-Assembled Multi-Electron-Acceptor Organic Molecule as High-Performance Cathode Material for Li-Ion Batteries

*Meng-Siou Wu,[ab] Teng-Hao Chen,[c] Hailong Lyu,[d] Te-Wei Huang,[e] Sheng Dai,[d] Xiao-Guang Sun,[d] Alexander S. Ivanov,[d] Jui-Chin Lee,[f] Ilja Popovs,[*d] and Watchareeya Kaveevivitchai[*ab]*

[a]*Department of Chemical Engineering, National Cheng Kung University, Tainan City 70101, Taiwan*

[b]*Hierarchical Green-Energy Materials (Hi-GEM) Research Center, National Cheng Kung University, Tainan City 70101, Taiwan*

[c]*School of Pharmacy, National Cheng Kung University, Tainan City 70101, Taiwan*

[d]*Chemical Sciences Division, Oak Ridge National Laboratory, Oak Ridge, P.O. Box 2008, TN 37831, USA*

[e]*Department of Chemistry, Tamkang University, New Taipei City 25137, Taiwan*

[f] *Instrument Center, National Cheng Kung University, Tainan City 70101, Taiwan*

*To whom correspondence should be addressed. E-mail: popovsi@ornl.gov (I. Popovs), wkaveechai@mail.ncku.edu.tw (W. Kaveevivitchai).

General methods and materials

The following starting materials and solvents were obtained from the respective commercial sources and used without further purification: dimethyl sulfoxide (DMSO, Sigma-Aldrich); glacial acetic acid (Sigma-Aldrich); octahydrate cyclohexane hexaketone (Sigma-Aldrich); nitric acid (Sigma-Aldrich); trifluoroacetic acid (TFA-*d*, Sigma-Aldrich); lithium bis(trifluoromethanesulfonyl)imide (LiTFSI, Sigma-Aldrich); 1,2-dimethoxyethane (DME, Sigma-Aldrich); 1,3-dioxolane (DOL, Acros-Organic); lithium nitrate ($LiNO_3$ Sigma-Aldrich); Ketjen black (Lion Specialty Chemicals); poly(vinylidenedifluoride) (PVDF, Sigma-Aldrich); poly(tetrafluoroethylene) (PTFE, Alfa Aesar); *N*-methyl-2-pyrrolidinone (NMP, Alfa Aesar); 1.0 M lithium hexafluorophosphate ($LiPF_6$) in 1:1 v/v ethylene carbonate (EC)/diethylene carbonate (DEC) (Sigma-Aldrich); carbon paper (MGL280, Fuel Cell Earth); copper powder (Sigma Aldrich). 2,3-Diamino-1,4-naphtaquinone was prepared from 2,3-dichloro-1,4-naphthoquinone by reacting it with phthalimide potassium salt in refluxing acetonitrile, followed by amine deprotection according to literature.[1]

Powder X-ray diffraction (PXRD) patterns were collected on Bruker D8 Advance ECO. Single-crystal X-ray diffraction experiments were performed by using Bruker D8 Venture dual X-ray single crystal diffractometer. X-ray photoelectron spectroscopy (XPS) measurements were performed on ULVAC PHI 5000 VersaProbe III with Al Kα (1487 eV) as an X-ray source. Survey scans were collected with a pass energy of 100 eV, followed by high-resolution scans of the C 1s, N 1s and O 1s regions with a pass energy of 20 eV. All spectra were charge-corrected relative to the C 1s component at 284.5 eV binding energy, and analyzed using CasaXPS software. The Raman spectra of the samples were collected by UniDRON Raman microscope with an excitation laser beam wavelength of 633 nm. Fourier-transform infrared (FT-IR) spectra were recorded on Nicolet iS5 or Nicolet 6700, Thermo Scientific. Scanning Electron Microscopy (SEM) images were collected on a SU8010 HR-FESEM scanning electron microscope. The electron paramagnetic resonance (EPR) spectra were recorded on a Bruker EMX System EPR with X-band EPR spectrometer operating at 9.80 GHz. Microwave power was set to 2.002 mW. Sweep width was performed with 100G and a center field of 3510G. The field modulation frequency was set to 100 kHz, and the modulation amplitude was 6G. Thermogravimetric analysis (TGA) was performed using TA Q50 instrument from 20 °C to 800 °C with a heating rate of 10 °C min^{-1} under nitrogen flow of 10 ml min^{-1}. High resolution mass spectrometric (HRMS) analysis results were acquired by the University of Texas at Austin Mass Spectrometry Facility. The ^1H nuclear magnetic resonance (NMR) spectrum was recorded on a Bruker AV-500.

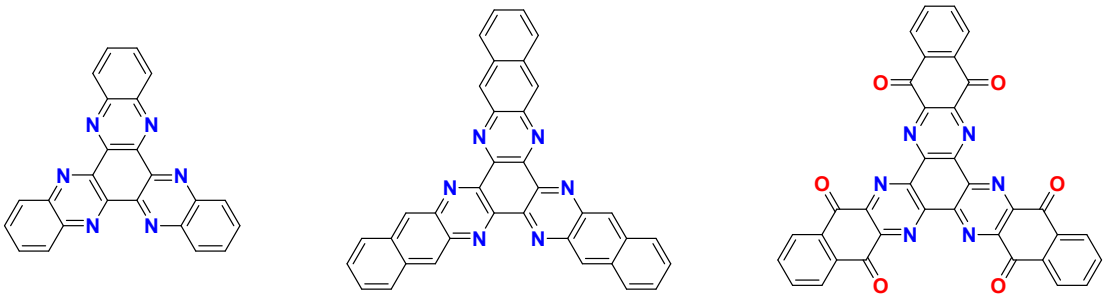

HAT or 3Q HATA HATAQ

Scheme S1. Chemical structures of (a) HAT, also known as 3Q, (b) HATA and (c) HATAQ.

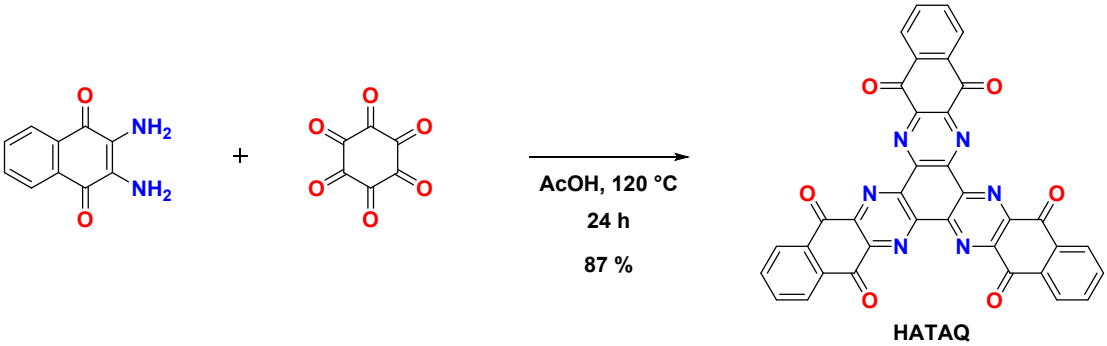

Scheme S2. Synthesis of HATAQ (benzo[i]benzo[6,7]quinoxalino[2,3-a]benzo[6,7]quinoxalino[2,3-c]phenazine-5,8,13,16,21,24-hexaone)

2,3-Diamino-1,4-naphtaquinone (61.2 g, 325 mmol) was dissolved in degassed glacial acetic acid (1500 mL). To this solution, cyclohexane hexaketone as an octahydrate (31.2 g, 100 mmol) was added in one portion. The reaction mixture was heated under reflux at 120 °C over 24 h period under the argon atmosphere. Upon reaction completion, the reaction mixture was cooled to 60 °C and the solid residue was recovered by filtration. The obtained dark brown solid was successively washed with fresh glacial acetic acid (200 mL), ethanol (200 mL), acetone (200 mL) and water (4 x 250 mL), and dried under vacuum over 24 h. The resulting black solid was suspended in 25 % nitric acid (250 mL). The obtained suspension was heated under reflux at 100 °C with vigorous stirring for 2 h. The color of suspension turned from dark brown to dark orange upon heating. The reaction mixture was cooled to room temperature and the solid was separated by filtration on glass filter. Filter cake was washed with deionized water (5 x 500 mL) followed by drying under dynamic vacuum overnight. Title product was obtained as a yellow-orange powder (54.3 g, 87% yield). ^{1}H NMR (500 MHz, TFA-*d*): 8.73-8.65 (m, 6H), 8.20-8.10 (m, 6H). HRMS (+ mode): Calculated m/z for $C_{36}H_{12}N_6O_6$ (M+H) 625.0891, observed 625.0878.

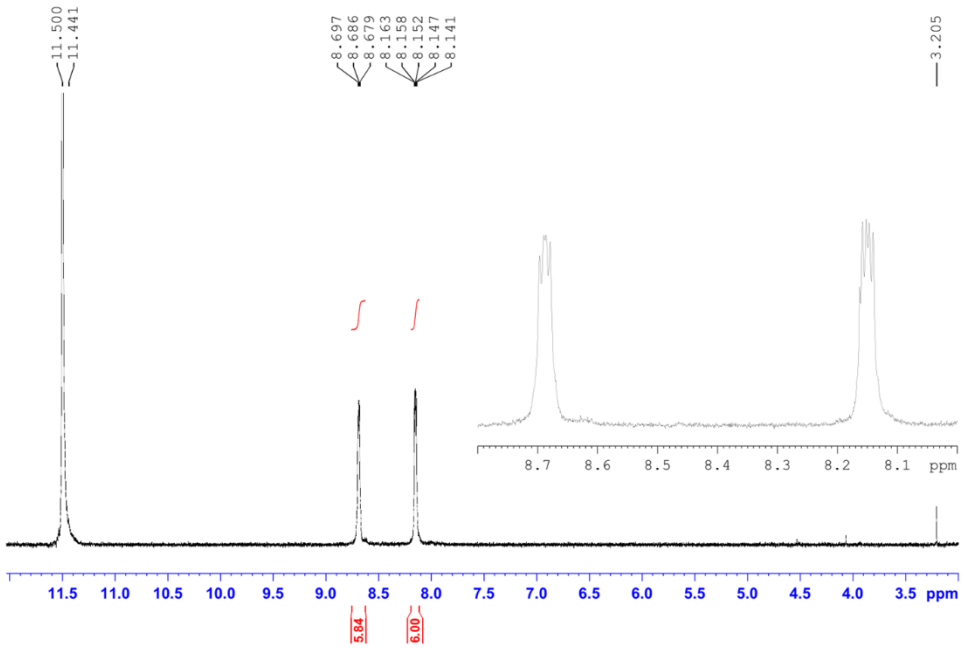

Figure S1. ^{1}H-NMR spectrum of HATAQ in TFA-d_1 solvent.

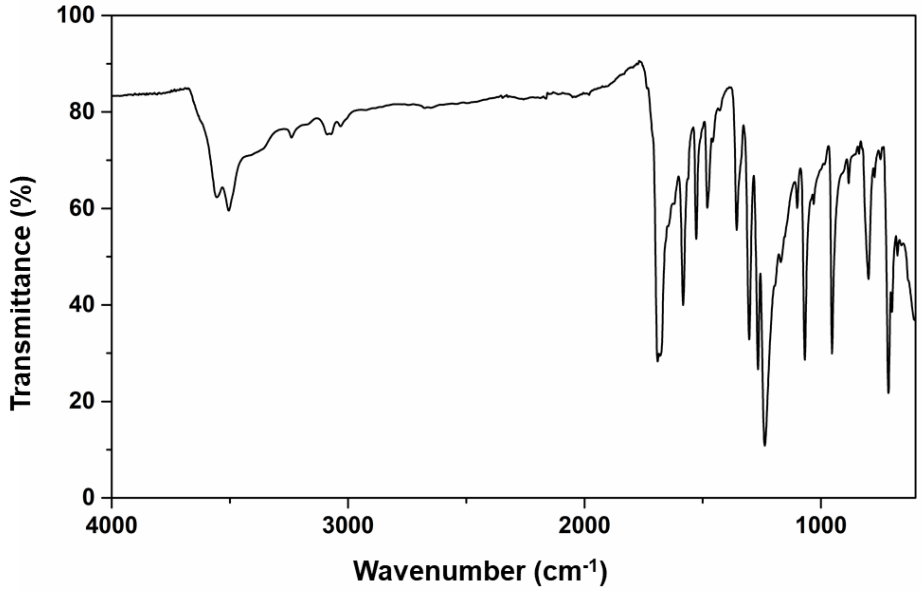

Figure S2. FT-IR spectrum of HATAQ.

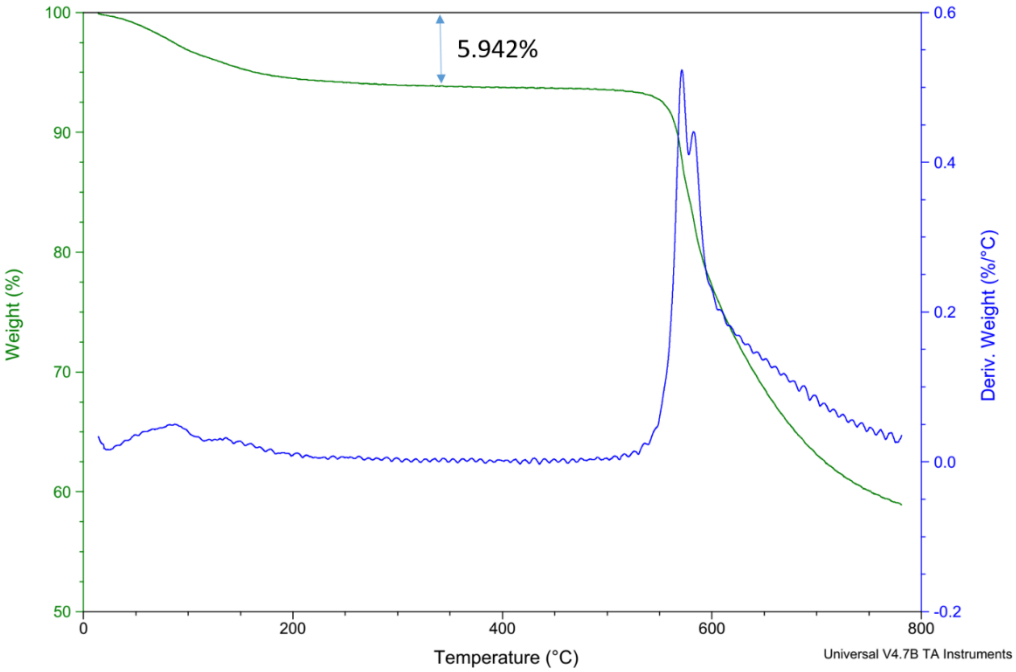

Figure S3. TGA plot of as-synthesized HATAQ sample under N_2. Rapid weight loss of around 5.94% corresponding to release of trapped water molecules is apparent with the onset of temperature reaching a plateau at 200 °C. Further Rapid weight loss takes place above 550 °C.

Crystallization of HATAQ

HATAQ (1.5 mg) and dimethyl sulfoxide (DMSO, 0.4 mL) were mixed in a 4 mL vial, and the suspension was sonicated for 5 min. The mixture was heated in a 140 °C oven for 2 h to obtain a clear solution. The solution was cooled down to 30 °C with a rate of 5 °C h^{-1} and yellow prism crystals were obtained.

Table S1. Crystallographic data of HATAQ.

Identification code	HAT DMSO
Empirical formula	C_{48} H_{48} N_6 O_{12} S_6
Formula weight	1093.28
Temperature/K	200(2)
Crystal system	Trigonal
Space group	R –3 c
a/Å	15.8095(9)
b/Å	15.8095(9)
c/Å	44.424(3)
α/°	90.00
β/°	90.00
γ/°	120
Volume/Å^3	9615.7(10)
Z	6
ρ_{calc} g/cm^3	1.133
μ/mm^{-1}	0.267
F(000)	3420
Radiation	Mo Kα (λ = 0.71073)
2*θ* range for data collection/°	2.36 to 25.06
Index ranges	-18 ≤ h ≤18, -18 ≤ k ≤ 16, -52 ≤ l ≤ 52
Reflections collected	43300
Independent reflections	1884 [R_{int} = 0.0781, R_{sigma} =0.0247]
Data/restraints/parameters	1884/1/114
Goodness-of-fit on F^2	1.734
Final *R* indexes [$I > 2\sigma(I)$]	R_1 = 0.1281, wR_2 = 0.3887
Final *R* indexes [all data]	R_1 = 0.1427, wR_2 = 0.4062
Largest diff. peak/hole / e Å^{-3}	0.895/–0.532

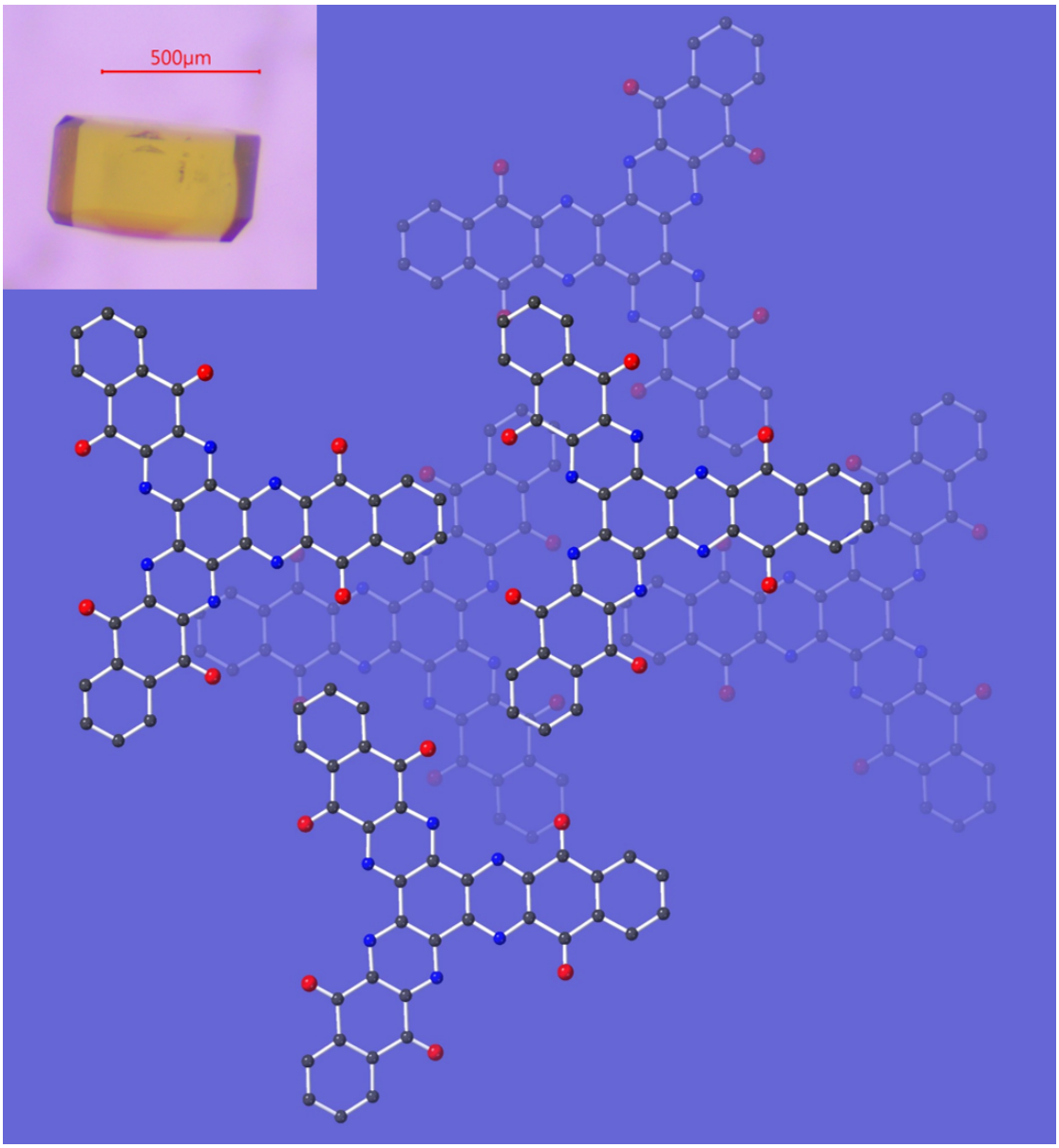

Figure S4. Single crystal (inset) and crystal structure of HATAQ (C, gray; N, blue; O, red; the hydrogen atoms and intercalated DMSO molecules are omitted for clarity).

Electrode mechanistic studies

The HATAQ electrodes for ex-situ and in-situ Raman measurements contained 40 wt% active material, 50 wt% copper and 10 wt% PVDF.[2] Stainless steel was used as current collector. CR2032 coin cells were assembled by using Li metal as anode, 1 M LiTFSI in DOL/DME (1:2 v/v) with 0.3 wt% $LiNO_3$ as electrolyte and Whatman glass microfiber membrane as separator. The electrodes for ex-situ FT-IR contained 30 wt% active material, 60 wt% copper and 10 wt% PTFE.[2] The self-standing electrodes (0.2 mm thick) were dried in vacuum overnight at 80 °C. The coin cells were assembled by using Li metal anode, 1 M $LiPF_6$ in EC/ DEC (1:1 v/v) electrolyte and Celgard separator. The ex-situ XPS and EPR measurements were done on HATAQ electrodes consisting of 40 wt% active material, 50 wt% Ketjen Black and 10 wt% PVDF. The mixture was coated on stainless steel. The coin cells were assembled by using Li metal, 1 M LiTFSI in DOL/DME (1:2 v/v) with 0.3 wt% $LiNO_3$ and Whatman glass microfiber as anode, electrolyte and separator, respectively. The electrodes for ex-situ PXRD contained 80 wt% active material, 10 wt% Ketjen Black and 10 wt% PTFE. After hand mixing with ethanol, the mixture was pressed by rolling machine (MTI, MSK-2150) to get 0.2 mm thick electrodes, and the electrodes were dried overnight at 120 °C in vacuum. CR2032 coin cells were assembled by using Li metal anode, 1 M LiTFSI DOL/DME (1:2 v/v) with 0.3 wt% $LiNO_3$ electrolyte solution and glass fiber separator. For all the ex-situ measurements, the electrodes were cycled to various states of charge and the cells were disassembled in an argon-filled glovebox. All the samples were handled without any exposure to air.

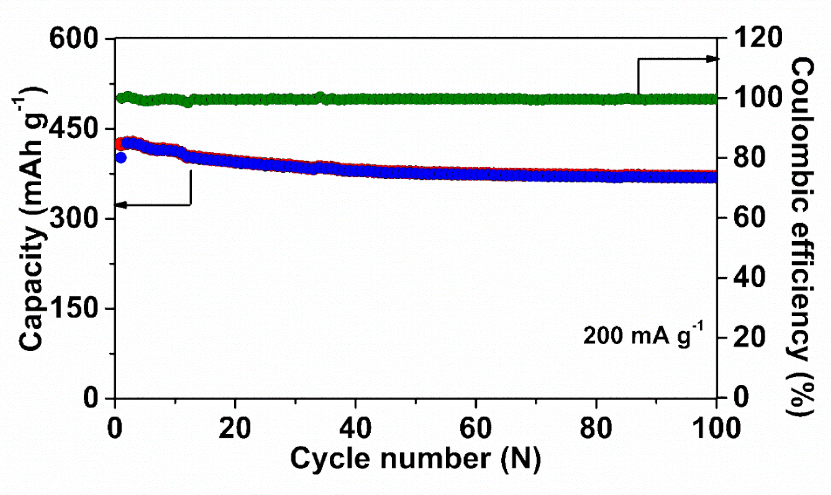

Figure S5. Capacity retention and coulombic efficiency of the HATAQ at 200 mA g^{-1} (0.4C) with 1 M LiTFSI 0.3 wt% $LiNO_3$ in 1:2 v/v DOL/DME as electrolyte (blue: discharge; red: charge).

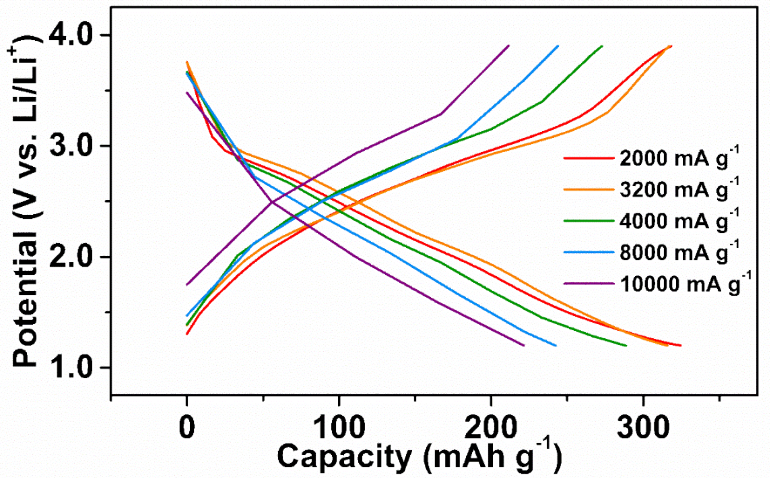

Figure S6. Discharge/charge profiles of the HATAQ electrodes at different current densities ranging from 2 A g^{-1} (4C) to 10 A g^{-1} (19C).

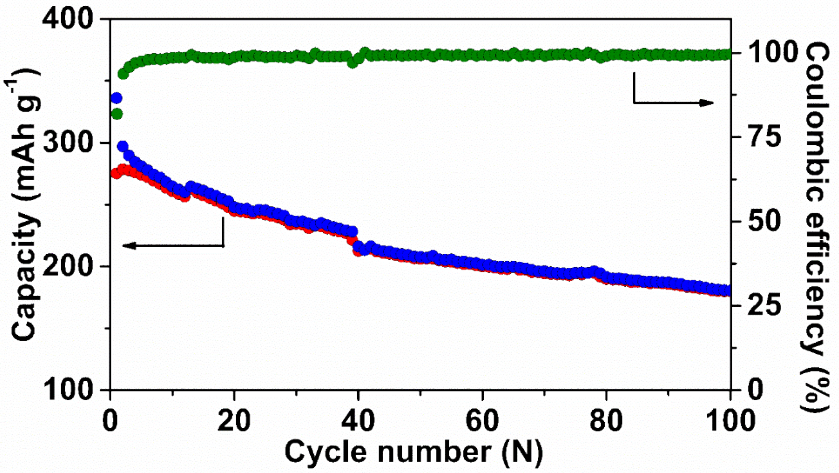

Figure S7. Cycling performance of the HATAQ electrode in a conventional Li-ion electrolyte, 1 M $LiPF_6$ in EC/DEC. The organic electrode material shows poor cycling performance due to the dissolution problem in the electrolyte (blue: discharge; red: charge).

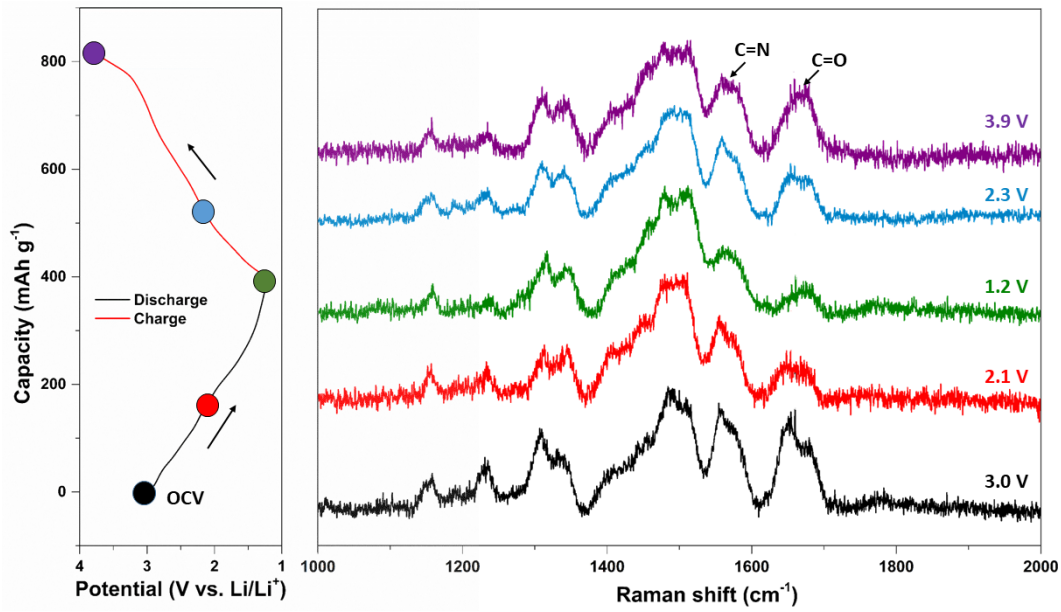

Figure S8. Ex-situ Raman spectra of the HATAQ electrodes for the first cycle in the voltage range of 1.2-3.9 V at 200 mA g^{-1}.

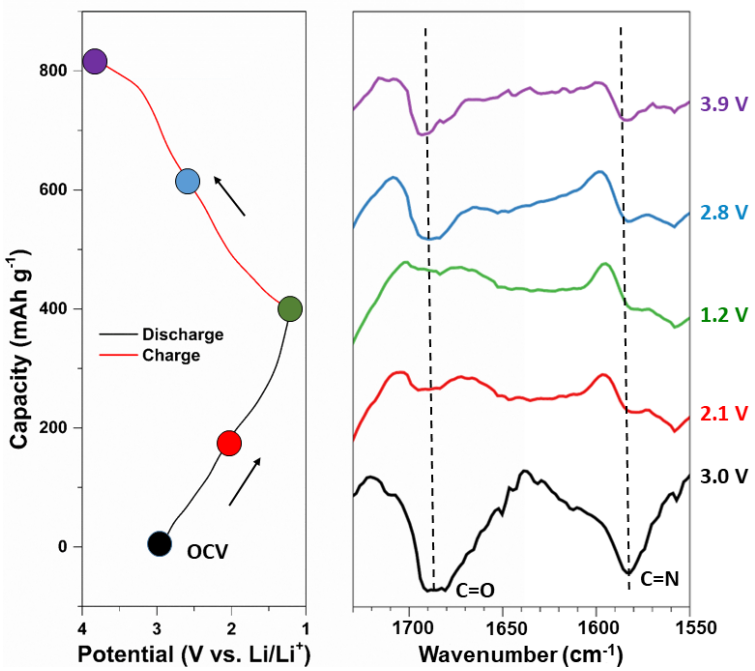

Figure S9. Ex-situ FT-IR spectra of the HATAQ electrodes at different charge/discharge states.

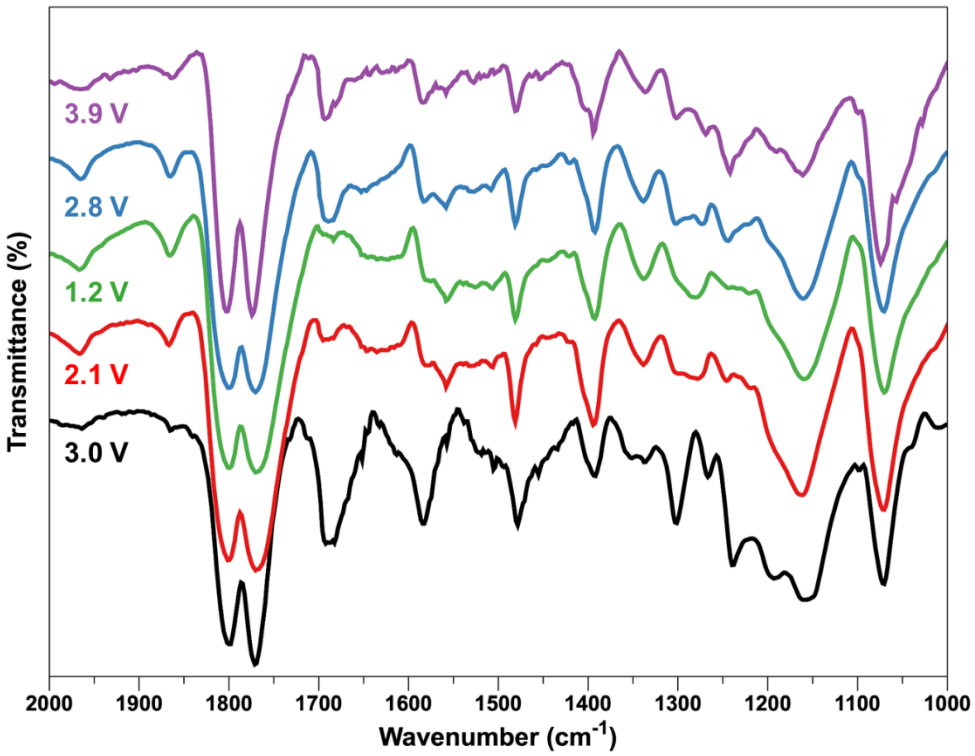

Figure S10. Ex-situ FT-IR spectra of the HATAQ electrodes at different states of charge (wavenumber of 1000-2000 cm^{-1}).

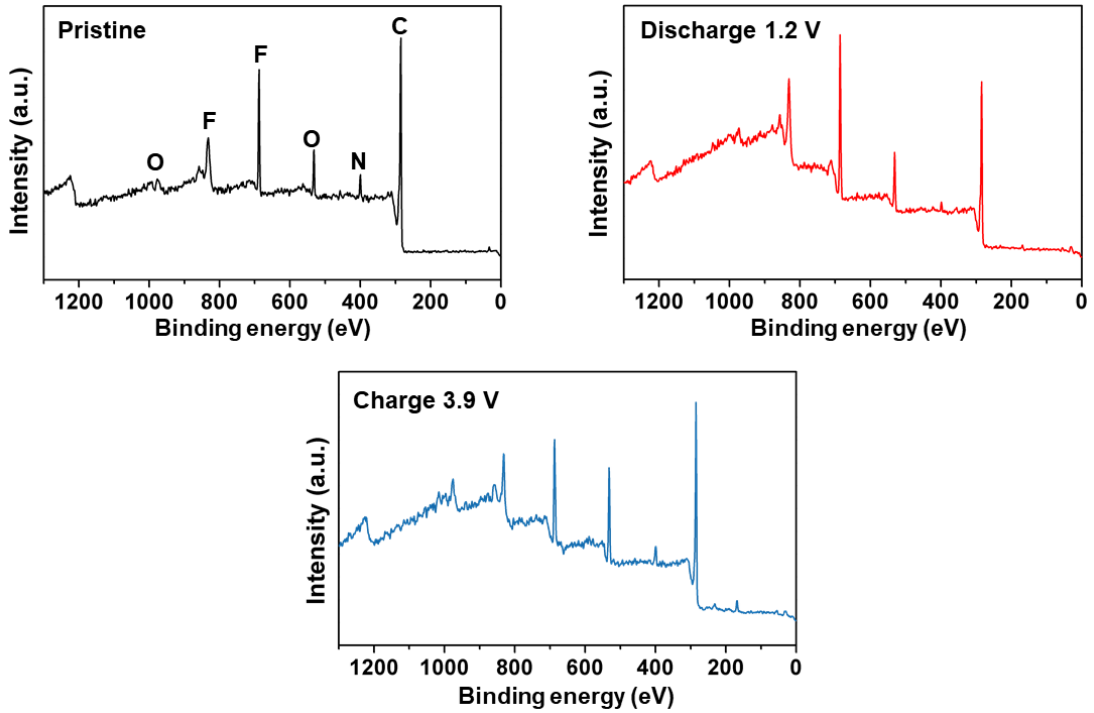

Figure S11. XPS low-resolution survey data of HATAQ electrodes at pristine state, discharged state at 1.2 V and charged state at 3.9 V, all indicating no impurities.

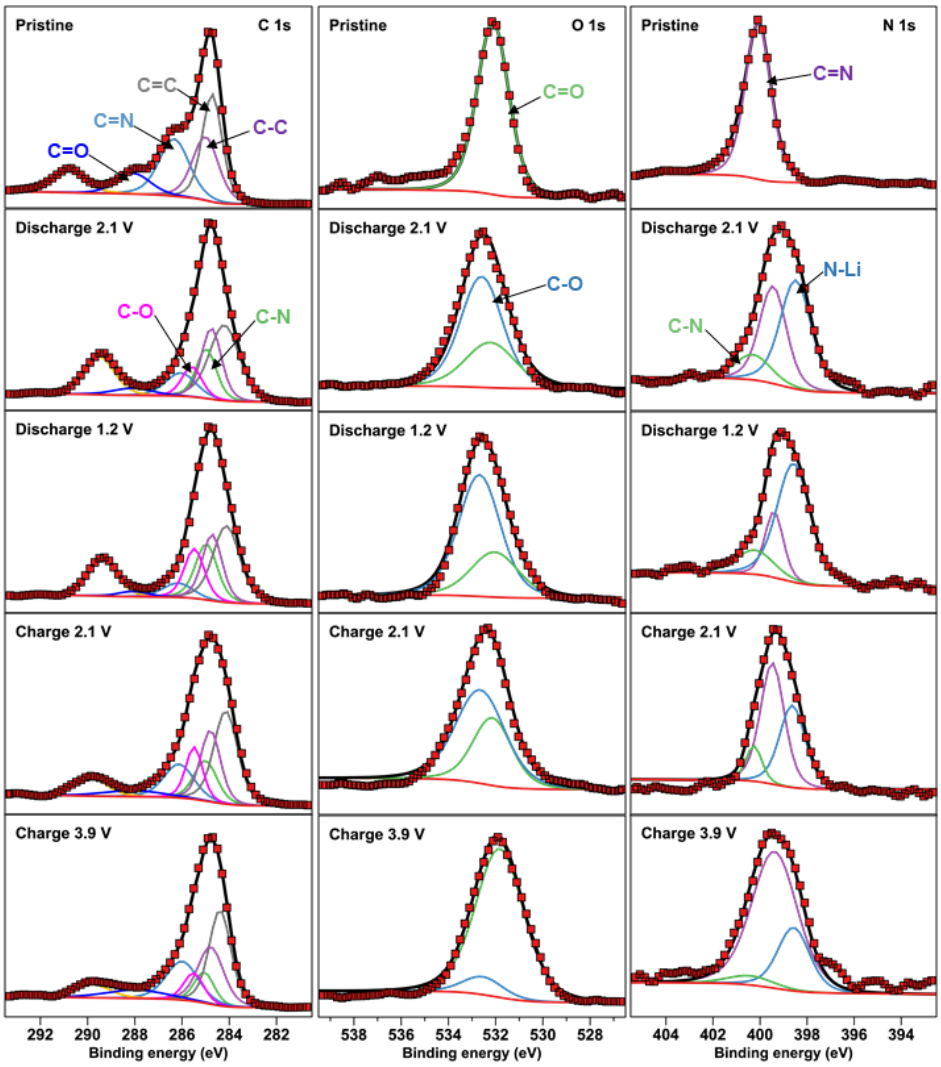

Figure S12. Deconvolution of the high-resolution XPS spectra of HATAQ electrodes at different states of charge: (Left) C 1s; (Middle) O 1s; (Right) N 1s.

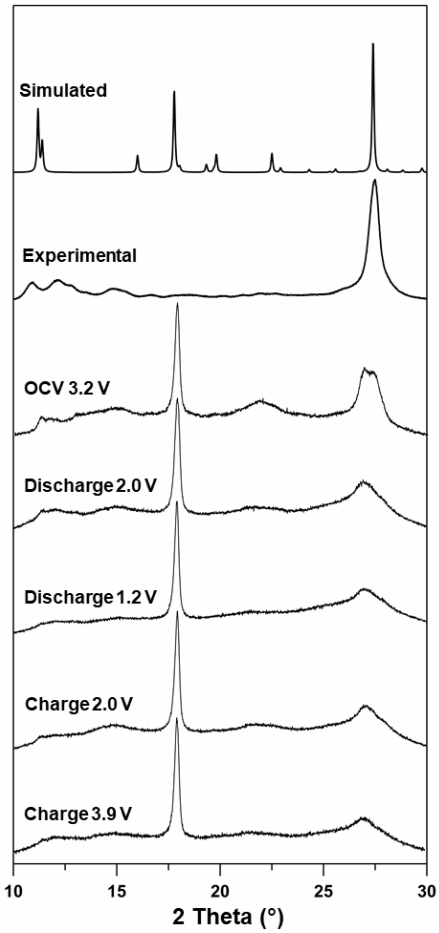

Figure S13. Top to bottom: Simulated PXRD pattern of solvent-free HATAQ; Experimental PXRD pattern of HATAQ powder after heating at 120 °C in vacuum; Ex-situ PXRD patterns of HATAQ electrodes at open circuit voltage (OCV); discharge to 2.0 and 1.2 V; followed by charge up to 2.0 and 3.9 V, respectively. The peak at approximately 18° belongs to PTFE polymer binder.

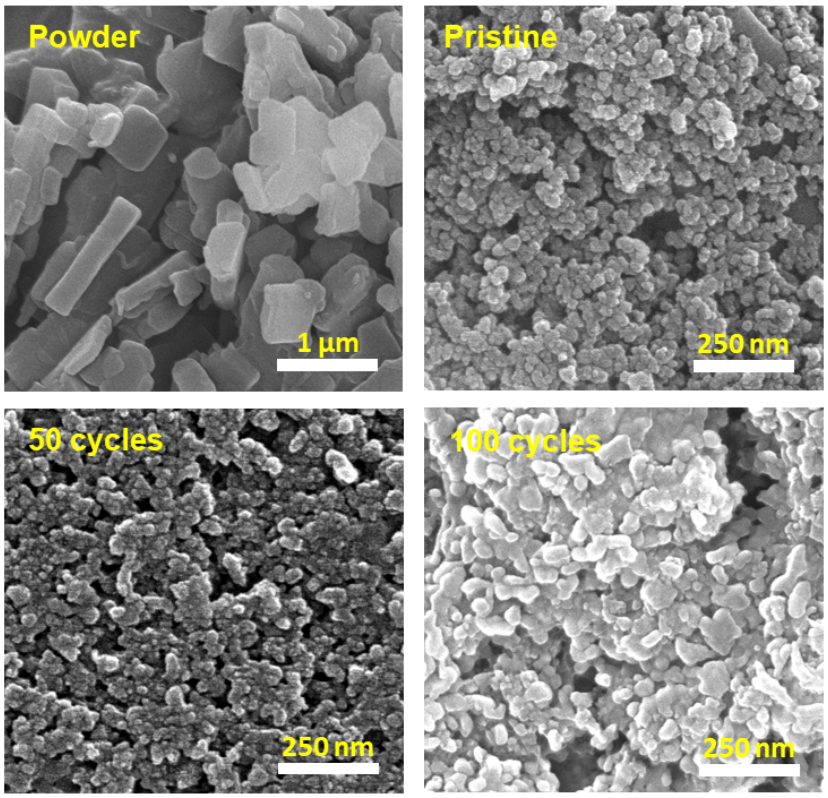

Figure S14. SEM images of HATAQ powder and electrodes: at OCV; after 50 cycles; and after 100 cycles (200 mA g^{-1}), showing that the morphology of the active material primarily remains unchanged after cycling.

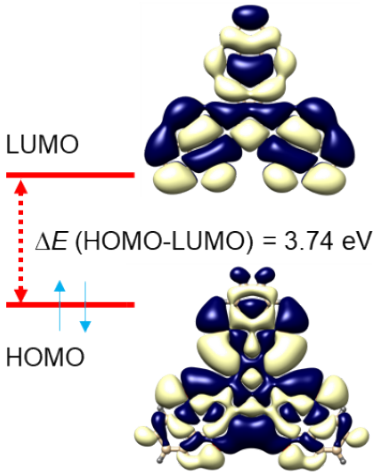

Figure S15. The lowest unoccupied (LUMO) and the highest occupied (HOMO) molecular orbitals (0.003 e/a_0^3 isovalue) and the corresponding HOMO-LUMO gap value (eV) for the HATAQ molecule calculated at the B3LYP/6-31+G(d,p)//IEF level of theory.

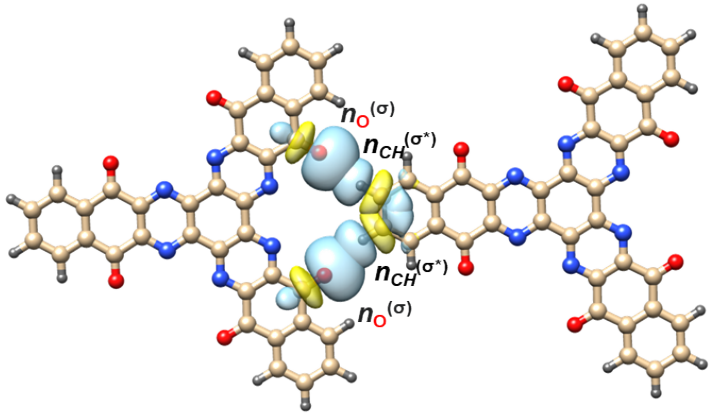

Figure S16. Lock-and-key C—H···O hydrogen bonds in the HATAQ dimer, characterized by overlap of the s-type oxygen lone pair ($n_O^{(\sigma)}$) and C—H σ* orbital.

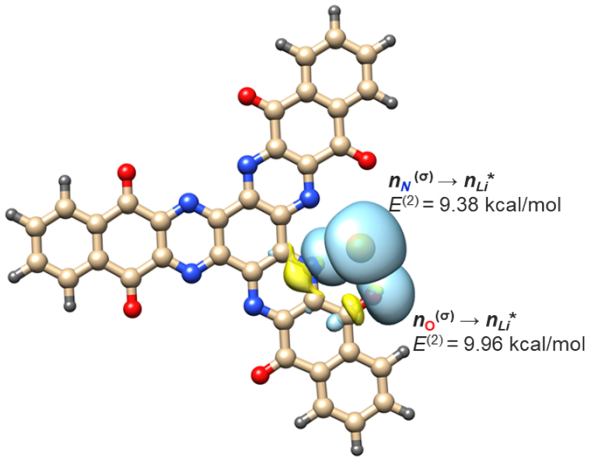

Figure S17. Comparison of principal NBO interactions in HATAQ-Li, associated with donation of O and N electron lone pairs into the vacant valence orbitals of Li to form two-center two-electron (2c-2e) Li ←:O and Li ←:N dative bonds. In this description the strength of donor–acceptor interactions in HATAQ-Li would be defined by the Lewis basicity/acidity of the components and can be estimated within the framework of second-order perturbation theory.[3] The obtained second-order stabilization energies, $E^{(2)}$ (kcal mol^{-1}), show almost equal contribution of O and N lone pairs to the Li binding.

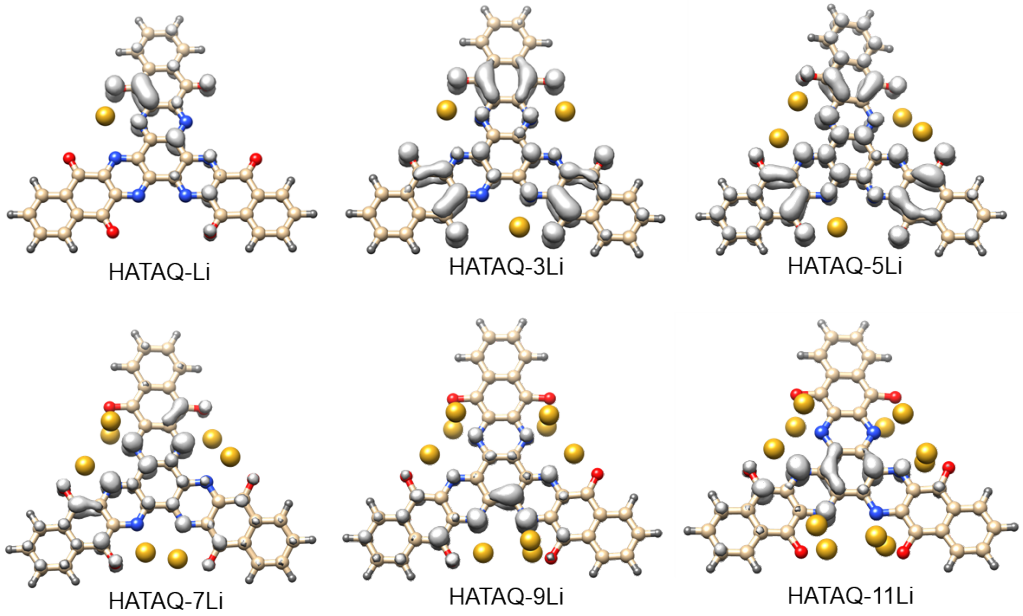

Figure S18. Calculated Mulliken spin densities for the HATAQ-Li complexes with an odd number of Li ions (one unpaired electron, doublet state). The spin density isosurfaces shown in grey are plotted using 0.003 e/a_0^3 isovalue. The spin densities are primarily delocalized over O and N atoms participating in Li chelation with some spin density residing on the aromatic rings due to π-conjugation.

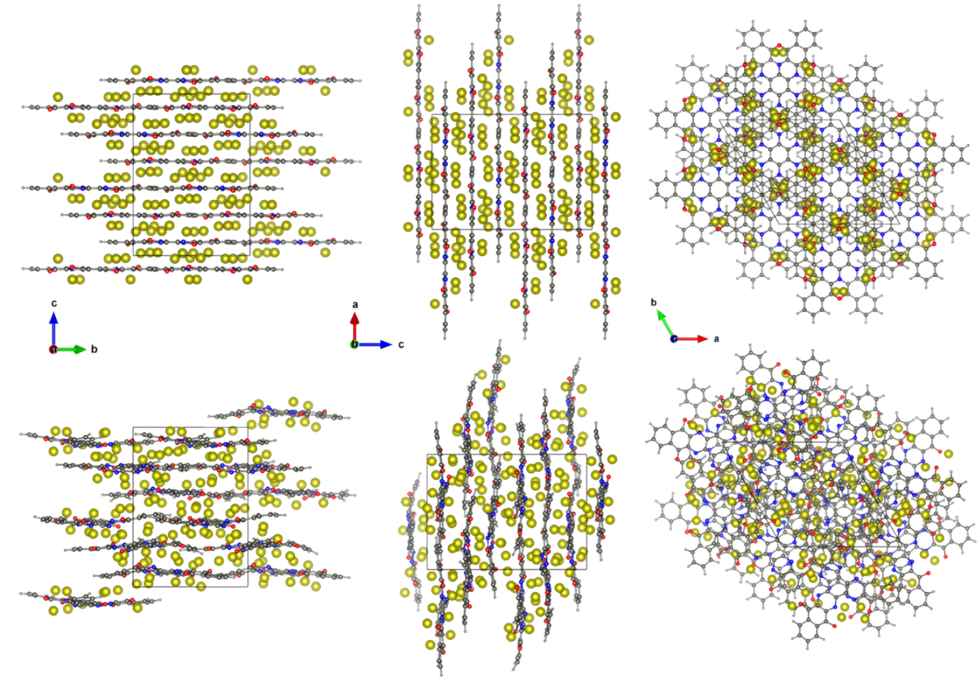

Figure S19. Structural changes of the fully lithiated HATAQ-12Li before (top) and after (bottom) 2 ps of *ab initio* molecular dynamics (MD) simulations at T = 400 K.

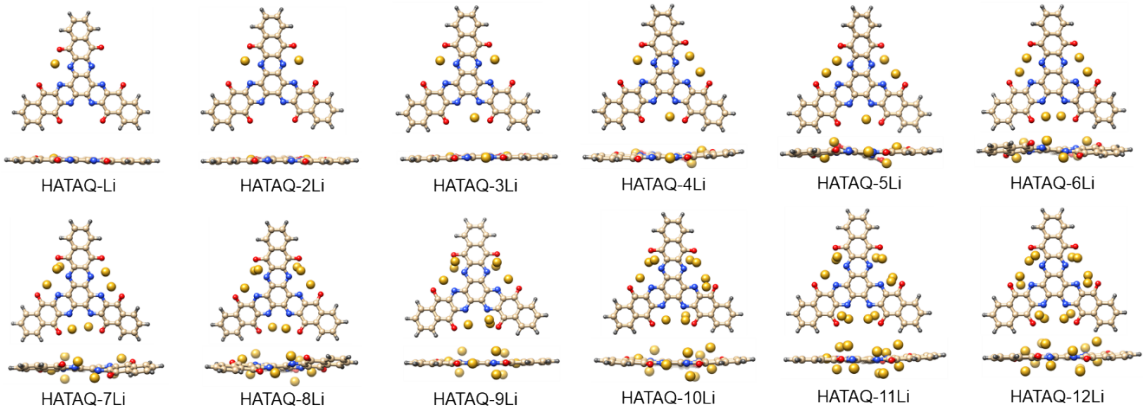

Figure S20. Top and side views of the DFT optimized global minimum structures for the HATAQ-*n*Li (*n* = 1-12) complexes.

Table S2. Calculated binding energies (BEs) and redox potentials at the B3LYP/6-31+G(d,p)//IEF level in DME solvent. BEs were calculated for the consecutive lithiation processes according to the following equation: BE = $E_{HATAQ\text{-}nLi} - (E_{HATAQ\text{-}(n\text{-}1)Li} + E_{Li})$, where $E_{HATAQ\text{-}nLi}$, $E_{HATAQ\text{-}(n\text{-}1)Li}$, and E_{Li} are the sum of electronic and zero-point energies (eV) of the final and initial lithiated states of the HATAQ molecule, and lithium atom, respectively; *n* is the number of Li/electrons transferred in the process.

Lithiation steps	**HATAQ→ HATAQ1Li**	**HATAQ1Li → HATAQ2Li**	**HATAQ2Li → HATAQ3Li**	**HATAQ3Li → HATAQ4Li**	**HATAQ4Li → HATAQ5Li**	**HATAQ5Li → HATAQ6Li**
BE, eV	-3.87	-3.69	-3.81	-2.99	-3.15	-2.77
Potential, V (vs. Li/Li$^+$)	3.51	3.36	3.41	2.60	2.79	2.35

Lithiation steps	**HATAQ6Li → HATAQ7Li**	**HATAQ7Li → HATAQ8Li**	**HATAQ8Li → HATAQ9Li**	**HATAQ9Li → HATAQ10Li**	**HATAQ10Li → HATAQ11Li**	**HATAQ11Li → HATAQ12Li**
BE, eV	-2.39	-2.10	-1.93	-1.58	-1.59	-1.41
Potential, V (vs. Li/Li$^+$)	2.10	1.73	1.61	1.25	1.24	1.07

Table S3. Lattice parameters of the HATAQ crystal structure obtained by X-ray diffraction and periodic DFT calculations.

	HATAQ		
Method	*a* (Å)	*b* (Å)	*c* (Å)
Experiment (X-ray diffraction)	15.8095(9)	15.8095(9)	44.424(3)
PBE-DFT-D3	15.5695	15.5695	44.6010

References

[1] J. Lee, H. Kim and M. J. Park, *Chem. Mater.*, 2016, **28**, 2408.
[2] S. Wu, W. Wang, M. Li, L. Cao, F. Lyu, M. Yang, Z. Wang, Y. Shi, B. Nan, S. Yu, Z. Sun, Y. Liu and Z. Lu, *Nat. Commun.*, 2016, **7**, 13318.
[3] A. E. Reed, L. A. Curtiss, F. Weinhold. *Chem. Rev.*, 1988, **88**, 899-926.